

Conductivity anisotropy and pseudogap in the microwave response of high- T_c superconductors

M R Trunin

DOI: 10.1070/PU2005v048n10ABEH005560

Contents

1. Introduction	979
2. Measurements of the impedance and conductivity anisotropies	980
2.1 Measured quantities and typical samples; 2.2 Geometrical factor in the T-orientation; 2.3 Electrodynamics of an anisotropic HTSC crystal; 2.4 Impedance and conductivity of $\text{YBa}_2\text{Cu}_3\text{O}_{6.93}$ single crystal; 2.5 Impedance anisotropy of $\text{YBa}_2\text{Cu}_3\text{O}_{7-x}$ at varying x	
3. Normal state	987
3.1 Normal skin effect; 3.2 Resistivity of the cuprate planes; 3.3 The c -axis resistivity	
4. Superconducting state	989
4.1 Surface impedance; 4.2 Complex conductivity; 4.3 Modified two-fluid model (MTFM); 4.4 On the residual surface resistance; 4.5 Inference concerning the impedance $Z_{ab}(T)$ and conductivity $\sigma_{ab}(T)$	
5. Pseudogap effect	993
5.1 Superfluid density $n_s(T, p)$; 5.2 The c -axis penetration depth $\lambda_c(T, p)$	
6. Conclusions	996
References	997

Abstract. Results of investigating the temperature dependences of the surface impedance $Z(T) = R(T) + iX(T)$ and complex conductivity $\sigma(T) = \sigma'(T) - i\sigma''(T)$ in the ab -planes and along the c -axis of high- T_c superconductors (HTSCs) are reviewed and critically analyzed. An electrodynamic method is considered for extracting all components of $\hat{\sigma}(T)$ and $\hat{Z}(T)$ tensors from quantities measured in microwave experiments. The main attention is focused on the evolution of $\hat{Z}(T)$ and $\hat{\sigma}(T)$ dependences in a $\text{YBa}_2\text{Cu}_3\text{O}_{7-x}$ crystal with the oxygen content variation. Possible mechanisms of conductivity are discussed in the framework of models for normal, superconducting, and pseudogap states of HTSCs.

1. Introduction

At present there are two highly topical problems concerning high- T_c superconductors (HTSCs): (i) the mechanisms of quasiparticle transport along crystallographic axes of these anisotropic compounds, and (ii) the nature and properties of pseudogap states in the HTSC phase diagram. Among the experimental methods of studying these problems are the measurements of the temperature dependences of the surface

impedance $Z(T) = R(T) + iX(T)$ in absolute units (Ohms) at microwave frequencies ω . The real part, the surface resistance $R(T)$, is related to the energy losses of an electromagnetic wave reflected from the superconductor and by the scattering mechanism of the normal carriers. The imaginary part, reactance $X(T)$, characterizes the response of the superconducting carriers. For local electrodynamics which applies to HTSCs, the impedance $Z(T)$ defines the complex conductivity $\sigma(T) = \sigma'(T) - i\sigma''(T) = \omega\mu_0/Z^2(T)$, where $\mu_0 = 4\pi \times 10^{-7} \text{ H m}^{-1}$. It is well known that precise measurements of $Z(T)$ in classical superconductors proved to be quite informative: the superconducting gap Δ was derived from the temperature dependence of the surface resistance $R(T) \propto \exp(-\Delta/k_B T)$ for $T < T_c/2$, the field penetration depth $\lambda(T)$ into a superconductor was derived from the reactance $X(T) = \omega\mu_0\lambda(T)$ for $T < T_c$, and the electron mean free path was determined by measuring $R(T)$ and $X(T)$ in the normal state ($T \geq T_c$). The applicability of the Bardeen–Cooper–Schrieffer (BCS) theory [1] to classical superconductors was clearly demonstrated by the nonmonotonic behavior (coherence peak) of the microwave conductivity $\sigma'(T)$ over the range $0.8 < T/T_c \leq 1$. However, even early studies of the impedance and conductivity of HTSC materials did not fit with the BCS theory: there was no coherence peak in $\sigma'(T)$ and, instead of exponential behavior at low temperatures, $Z(T)$ exhibited power-law temperature dependence.

In HTSCs, the values of Z and σ are characterized by two components: Z_{ab} and σ_{ab} in the weakly anisotropic CuO_2 ab -planes, and Z_c and σ_c across the cuprate planes. The small part of the HTSC phase diagram, corresponding to the optimal doping $p \approx 0.16$ (p is the hole concentration per copper atom in the CuO_2 plane) and maximum values of the

M R Trunin Institute of Solid State Physics, Russian Academy of Sciences, 142432 Chernogolovka, Moscow region, Russian Federation
Tel. (7-095) 993 47 47 (ext. 229 42)
Fax (7-252) 497 01
E-mail: trunin@issp.ac.ru

Received 7 April 2005
Uspekhi Fizicheskikh Nauk 175 (10) 1017–1037 (2005)
Translated by M R Trunin; edited by A Radzig

critical temperature $T_c = T_{c,\max}$, is the most extensively studied area. In the normal state for optimally doped HTSCs, the resistivity $\rho_{ab}(T) = 1/\sigma_{ab}(T)$ of the cuprate ab -planes increases proportionally to temperature, viz., $\Delta\rho_{ab}(T) \propto T$. The resistivity $\rho_c(T)$ in the perpendicular direction substantially exceeds the value of $\rho_{ab}(T)$ and also exhibits metallic behavior (the derivatives of $\rho_{ab}(T)$ and $\rho_c(T)$ with respect to temperature are positive). However, $\text{Bi}_2\text{Sr}_2\text{CaCu}_2\text{O}_8$ (BSCCO) compound, which is the most anisotropic HTSC (having $\rho_c/\rho_{ab} \approx 10^5$ at $T \approx T_c$ and $p \approx 0.16$), represents an exception: its resistivity $\rho_c(T)$ increases as T approaches T_c ($d\rho_c(T)/dT < 0$). This BSCCO feature agrees with the estimate of the minimal metallic conductivity in the c -direction for the anisotropic three-dimensional (3D) Fermi liquid model [2]:

$$\sigma_{c,\min}^{3D} = \sqrt{\frac{\rho_{ab}}{\rho_c}} \frac{ne^2 d^2}{h}, \quad (1)$$

where $n \approx 10^{21} \text{ cm}^{-3}$ is a 3D carrier concentration, d is the lattice constant along the c -axis, and h is the Planck constant. In BSCCO, the conductivity $\sigma_c = 1/\rho_c \ll \sigma_{c,\min}^{3D}$ at $T = T_c$, but the other optimally doped HTSCs possess $\sigma_c(T_c) > \sigma_{c,\min}^{3D}(T_c)$. Note that the conductivity $\sigma_{c,\min}$ in Eqn (1) is less than the Ioffe–Regel limit $\sigma_{\text{IR}} = e^2 k_F / h$ for the two-dimensional (2D) case, i.e., $\sigma_{c,\min} \approx \sqrt{\rho_{ab}/\rho_c} \sigma_{\text{IR}} d/a \ll \sigma_{\text{IR}}$ ($a \approx 2\pi/k_F$ is the lattice constant in the CuO_2 plane), whereas $\sigma_{ab,\min} \approx \sigma_{\text{IR}}$ [2].

A measure of HTSC anisotropy in the superconducting state is the ratio between the superfluid densities in the cuprate planes and perpendicular to them, which equals $\sigma_{ab}''(0)/\sigma_c''(0) = \lambda_c^2(0)/\lambda_{ab}^2(0)$, where σ_{ab}'' and σ_c'' are the imaginary parts of conductivity, and λ_{ab} and λ_c are the penetration depths of the high-frequency field for currents running in the ab -planes and perpendicular to them, respectively. It is common knowledge that $\Delta\lambda_{ab}(T) \propto T$ for $T < T_c/3$ in high-quality optimally doped HTSC crystals and this experimental fact provides strong evidence for $d_{x^2-y^2}$ symmetry of the order parameter in these materials [3]. However, there is no consensus in scientific literature about $\Delta\lambda_c(T)$ behavior at low temperatures. Even $\text{YBa}_2\text{Cu}_3\text{O}_{6.95}$ (YBCO, $T_c \approx 93 \text{ K}$), the most thoroughly studied single crystals, have shown both linear [4–6], $\Delta\lambda_c(T) \propto T$, and quadratic [7] dependences in the range $T < T_c/3$.

Another important feature of the microwave response of optimally doped HTSC crystals is the linear variation with temperature of the surface resistance $R_{ab}(T)$ in the ab -planes at low temperatures. At frequencies of about 10 GHz and below, the T -dependence of $\Delta R_{ab}(T)$ in tetragonal BSCCO [8–11], $\text{Ti}_2\text{Ba}_2\text{CaCu}_2\text{O}_{8-\delta}$ (TBCCO) [12], and $\text{Ti}_2\text{Ba}_2\text{CuO}_{6+\delta}$ (TBCO) [13–15] single crystals is linear over the range $0 < T \lesssim T_c/2$. For orthorhombic YBCO crystals, $\Delta R_s(T) \propto T$ for $T < T_c/3$ and $R_{ab}(T)$ displays a broad peak at higher temperatures [16–24]. This peak can be understood in terms of a competition between an increase in the quasiparticle lifetime and a decrease in the quasiparticle density as the temperature is lowered. The sufficiently slow decrease in the quasiparticle density is indicative of a highly anisotropic or unconventional order parameter, resulting in a very small or vanishing energy gap, while the increase in the quasiparticle lifetime is attributed to the presence of inelastic scattering which can be due to (i) the exchange interaction of antiferromagnetic spin fluctuations

[25], which would naturally lead to d -wave pairing, or (ii) a strong electron–phonon interaction [26–28] within the anisotropic s -wave pairing model [29, 30]. Moreover, there have been suggestions of unconventional states for describing the charge carriers in the CuO_2 planes, like the marginal Fermi liquid [31, 32] and the Luttinger liquid [33, 34]. However, to fit the data relevant to YBCO, the inelastic scattering time must increase with decreasing temperature much faster than predicted by any of these microscopic models. Furthermore, the d -wave model with point scatterers does predict a finite low-temperature and low-frequency limit which is independent of the concentration and the strength of the scattering centers [35]. The value of this universal surface resistance $R_{\text{res}} \equiv R_{ab}(T \rightarrow 0)$ is much lower than the R_{res} values obtained from experiments. There is no microscopic theory explaining the linear temperature dependence of $\Delta R_{ab}(T)$ up to $T = T_c/2$ in crystals with a nonorthorhombic structure and the shoulder in the curve $R_{ab}(T)$ observed in optimally doped YBCOs [21, 22] for $T > 40 \text{ K}$. Only for high-quality YBCO films does the d -wave theory come close to the experimental results obtained at a certain finite frequency, when the scattering phase shift was used as a fitting parameter [36]. In the absence of a microscopic theory, a modified two-fluid model has been suggested [37, 38], which adequately describes all peculiarities of the temperature dependences of the surface impedance in the ab -planes of HTSC single crystals with different chemical compositions.

Pseudogap states, appearing when $p < 0.16$, occupy a wide domain in the HTSC phase diagram, which is far less investigated. Measurements of the ac -susceptibility of oriented HTSC powders for $T < T_c$ show [39] $\sigma_c''(T)/\sigma_c''(0)$ dependences having smaller slope as $T \rightarrow 0$ than $\sigma_{ab}''(T)/\sigma_{ab}''(0)$. The normal state of underdoped HTSCs is characterized by the nonmetallic behavior of the resistivity $\rho_c(T)$ as T approaches T_c , by deviation of the ab -plane resistivity from its linear dependence $\Delta\rho_{ab}(T) \propto T$, and by the ρ_c/ρ_{ab} ratio rising dramatically with a decrease in concentration p . Many theoretical models have been proposed to explain these properties, but none describes the evolution of the dependences $\sigma_{ab}''(T)$, $\sigma_c''(T)$ and $\rho_{ab}(T)$, $\rho_c(T)$ in a wide range of concentrations and temperatures.

In the present review, we discuss the common and distinctive features of the temperature dependences of surface impedance $Z(T) = R(T) + iX(T)$ and complex conductivity $\sigma(T) = \sigma'(T) - i\sigma''(T)$ in the ab -planes and along the c -axis in the normal and superconducting states of HTSC single crystals. An electrodynamic method is considered in detail for determining all components of conductivity and impedance tensors on the base of measured microwave quantities. We analyze mainly the measurements of anisotropy and evolution of the temperature dependences of the conductivity components in $\text{YBa}_2\text{Cu}_3\text{O}_{7-x}$ crystal with the oxygen deficiency varied in the range $0.07 \leq x \leq 0.47$, and also give a universal approach to the solution to both problems mentioned above.

2. Measurements of the impedance and conductivity anisotropies

2.1 Measured quantities and typical samples

In the centimeter and millimeter wavelength ranges, the surface impedance of small-sized HTSC samples with a

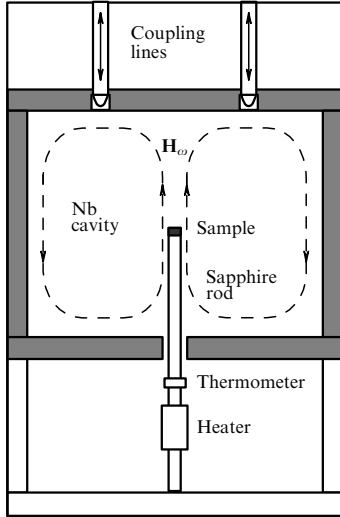


Figure 1. Schematic of the microwave cavity utilized in the 'hot-finger' technique.

surface area $\sim 1 \text{ mm}^2$ is measured by the so-called hot-finger method [40]. A sample mounted on a sapphire rod was placed at the center of a cylindrical cavity made from Nb and operating at the frequency $f = 9.42 \text{ GHz}$ in the H_{011} mode [41], i.e., the sample was placed in the maximum of a quasi-uniform microwave magnetic field (Fig. 1). The temperature of the rod and the sample was varied from liquid-helium temperature to room temperature without heating the cavity itself, which was washed from outside by liquid helium and was always in the superconducting state. At some steady-state temperature T , the microwave power conveyed through the cavity was recorded as a function of frequency (resonance curve), from which was derived, in the first run, the Q -factor $Q_s(T)$ and the frequency $f_s(T)$ of the cavity with the sample inside and, in the second run, $Q_e(T)$ and $f_e(T)$ of the cavity without the sample. The temperature dependences of the surface resistance R and reactance X of the sample are found from the relationships [41]

$$R(T) = \Gamma \Delta Q^{-1} = \Gamma [Q_s^{-1}(T) - Q_e^{-1}(T)], \quad (2)$$

$$X(T) = -2\Gamma \frac{\delta f}{f} = -\frac{2\Gamma}{f} (\Delta f_s(T) - \Delta f_e(T) - f_0), \quad (3)$$

where Γ is the geometrical factor of the sample, and δf is the frequency difference of the cavity with the sample and the cavity with an ideal conductor, identical in shape and size, into which the magnetic field does not penetrate. The δf value deviates from the difference between the measured resonance frequency shifts $\Delta f_s - \Delta f_e = \Delta f$ by a constant f_0 which accounts for both the frequency drift caused by the ideal conductor and changes that are not reproducible in the cavity reference frequency upon putting in and taking out the sample. It follows from Eqns (2) and (3) that for determining the $R(T)$ and $X(T)$ values from the measured $Q(T)$ and $\Delta f(T)$ values, two quantities need to be known: Γ and f_0 . In HTSC single crystals, the f_0 constant can be determined from the measurements of the microwave response in the normal state (see Section 2.3). The geometrical factor of the sample (by order of magnitude, it is equal to dozens of kilohms at frequencies $\sim 10 \text{ GHz}$) depends on the shape and size of the

crystal and on its orientation in the cavity:

$$\Gamma = \frac{2\omega W}{\gamma}, \quad W = \frac{\mu_0}{2} \int_V H_\omega^2 dV, \quad \gamma = \int_s H_t^2 ds, \quad (4)$$

where W is the energy stored in the cavity, V is the volume of the cavity, H_ω is the microwave magnetic field generated in the cavity, s is the total sample surface area, and H_t is the tangential component of H_ω on the sample surface. The energy W is easily evaluated for the resonator mode under use, and the task of deriving the impedance value is reduced to taking the integral γ in formula (4).

The task is simplified if a typical HTSC crystal in the form of a long, thin rectangular plate with dimensions $b \gg a > c$ and volume $v \sim 0.1 \text{ mm}^3$ is radiated by the microwave magnetic field $H_\omega \parallel b$ (L-orientation, Fig. 2a). If this is the case, in the superconducting state for $T < 0.9 T_c$, when the magnetic field penetration depth is smaller than the characteristic sample dimensions, the quantity $H_t \simeq H_0$ can be taken outside the integral sign of γ , where H_0 is an amplitude of H_ω . Thus, we obtain $\gamma \approx 2H_0^2(ab + bc)$, so the surface impedance Z_{ab+c} for the sample in the L-orientation will be equal to

$$Z_{ab+c} \approx \frac{abZ_{ab} + bcZ_c}{ab + bc}, \quad (5)$$

where the subscripts of Z stand for the directions of the screening currents. While deriving formula (5) we neglected the weak anisotropy in the ab -plane and the contribution of the crystal ac -faces, which is apparently minute in comparison with the summands in the numerator of formula (5) due to the area difference: $ac \ll bc < ab$. Cleaving of the crystal along the bc -face into several needles multiplies the contribution from the c -currents, so that measurements of Z_{ab+c} before and after the cleaving allow, in principle, one to extract Z_c in the superconducting state of $\text{YBa}_2\text{Cu}_3\text{O}_{6.95}$ single crystal using Eqn (5). In Ref. [7], this procedure was

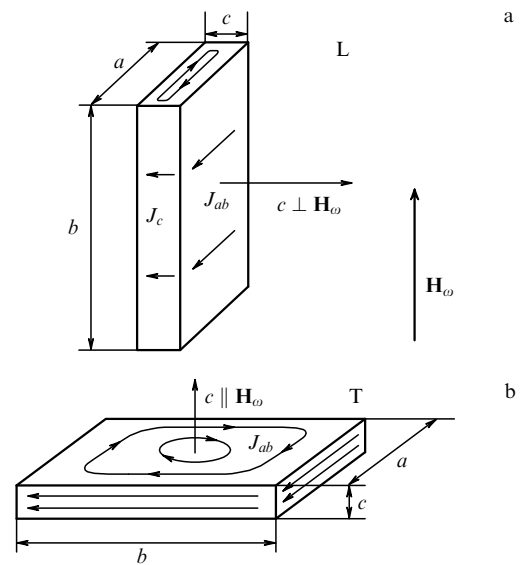


Figure 2. Two experimental orientations of the sample with respect to the microwave magnetic field H_ω in the cavity: (a) longitudinal (L) orientation, $c \perp H_\omega$, and (b) transverse (T) orientation, $c \parallel H_\omega$. Arrows indicate the directions of the high-frequency currents.

suggested as an optimal one for determining Z_c in the superconducting state of $\text{YBa}_2\text{Cu}_3\text{O}_{6.95}$ crystal. However, it involves the following disadvantages: (i) it assumes the abZ_{ab} term in Eqn (5) to be unalterable, which results in an uncontrolled inaccuracy due to nonideal sample cleaving into rectangular needles, (ii) formula (5) is not valid at temperatures $T > 0.9 T_c$ because of the size effect which, as will be shown in Sections 2.3 and 2.4, plays an essential role even for the case of weak anisotropy in YBCO, and (iii) cleaving of the crystal excludes the opportunity for its further study, in particular for investigating the microwave response evolution during changes in the doping level in the same sample. Therefore, consecutive measurements in the crystal at first in transverse (T) orientation $\mathbf{H}_\omega \parallel c$ (Fig. 2b) to find Z_{ab} , and then in the longitudinal one appear to be a more natural way to obtain Z_c . A difficulty in determining the geometrical factor Γ or the integral γ in Eqn (4) in the T-orientation of the crystal arises, however, while applying this technique. As mentioned in Ref. [41], $\gamma \approx 2H_0^2 a^2 (\ln(a/c) + 1)$ proves to be a reasonable estimate for a square sample with $a = b \gg c$. It is also known that the approximation of a rectangular plate by an ellipsoid inscribed in it results in an overestimated value of γ .

2.2 Geometrical factor in the T-orientation

Let us consider an ideal prolate rectangular conductor with dimensions $L_y \gg L_x, L_z$, placed in a constant magnetic field $\mathbf{H} \parallel z$. The problem of obtaining the field distribution around such a conductor becomes two-dimensional and has been solved in Ref. [6]. The upper inset to Fig. 3 displays the distribution of the $H_z(z)$ and $H_x(x)$ magnetic field components in the $L_z L_y$ - and $L_x L_y$ -planes, respectively, for three different L_z/L_x ratios. General expressions for the magnetic moment M of the conductor and the integral γ in Eqn (4) have

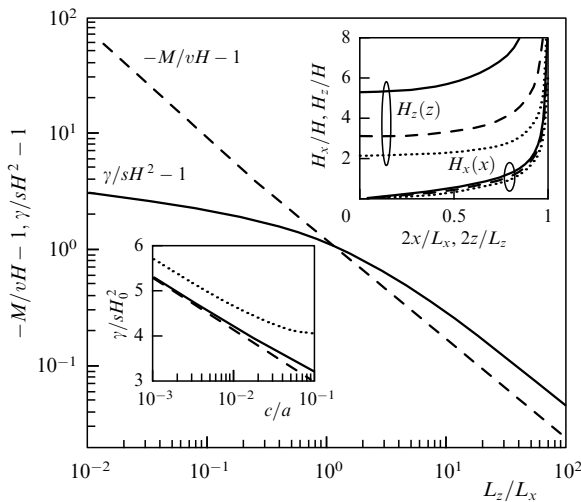


Figure 3. The values of $(-M/vH - 1)$ (dashed line) and $(\gamma/sH^2 - 1)$ (solid line) calculated from Eqns (6) and (7) versus the ratio L_z/L_x in a rectangular superconducting plate with dimensions $L_y \gg L_x, L_z$, placed in a constant magnetic field $\mathbf{H} \parallel z$. The upper inset represents the magnetic field distributions on the surfaces $L_z L_y$ (upper three curves) and $L_x L_y$ (lower curves) for the values of $L_z/L_x = 0.25$ (dotted line), 0.1 (dashed line), and 0.03 (solid line). The lower inset depicts γ/sH_0^2 as a function of c/a . Solid and dashed lines correspond to the calculated results obtained by Eqn (7) and Eqn (10), respectively. The dotted line is the upper bound of γ/sH_0^2 estimated from Eqn (11) for $b = 4a$.

the following forms [6]

$$-\frac{M}{L_y H} = \frac{4}{H} \left(\int_0^{L_x/2} x |H_x| dx + \frac{L_x}{2} \int_0^{L_z/2} H_z dz \right) = \frac{\pi(1-k^2)L_z^2}{4} (E(k) - (1-k^2)K(k))^2, \quad (6)$$

$$\frac{\gamma}{L_y H^2} = \frac{4}{H^2} \left(\int_0^{L_x/2} H_x^2 dx + \int_0^{L_z/2} H_z^2 dz \right) = 2(L_x f_x + L_z f_z), \quad (7)$$

where

$$f_x = \frac{K(\sqrt{1-k^2}) - E(\sqrt{1-k^2})}{E(\sqrt{1-k^2}) - k^2 K(\sqrt{1-k^2})},$$

$$f_z = \frac{E(k)}{E(k) - (1-k^2)K(k)}, \quad (8)$$

with $K(v)$ and $E(v)$ being complete elliptic integrals of the first and second kinds. Formula (6) coincides with the result obtained previously in Ref. [42]. Furthermore, the relationship between the ratio L_z/L_x and k is required for calculating the values of the moment M/v ($v = L_x L_y L_z$ is a conductor volume) and the factor γ/s [$s = L_y(L_z + L_x)$ is a conductor surface area]:

$$\frac{L_z}{L_x} = \frac{E(k) - (1-k^2)K(k)}{E(\sqrt{1-k^2}) - k^2 K(\sqrt{1-k^2})}. \quad (9)$$

Then, $(-M/vH - 1)$ and $(\gamma/sH^2 - 1)$ dependences on the L_z/L_x ratio, computed from formulae (6) and (7), are represented in Fig. 3. If $L_z \gg L_x$, the magnitude of the magnetic field on the sample surface tends to that of the applied one along with the values of M and γ tending to $(-vH)$ and sH^2 , respectively.

Presently, we apply the formulae (6)–(9) to determine the geometrical factor of an HTSC crystal transversely placed with respect to the \mathbf{H}_ω field (Fig. 2b) in the cavity. The field distribution over the ideal conductor surface will coincide with alternating magnetic field distribution over the surface of a superconducting sample with the same dimensions ($L_x = a, L_y = b, L_z = c$) placed in microwave field $\mathbf{H}_\omega = \mathbf{H}$, provided that the field penetration depth is smaller than the sample dimensions. It is easy to arrive at a simple estimate of γ in the case of a very thin crystal ($c \ll a \ll b$). Upon keeping the first term in the series expansion in terms of the $k \ll 1$ on the right-hand side of Eqn (9), we get the relationship $k \approx \sqrt{4L_z/\pi L_x}$. Therefore, small values of k correspond to $c/a \ll 1$. The subsequent substitution of $k = \sqrt{4c/\pi a}$ into asymptotic forms $f_x(k) \approx K(\sqrt{1-k^2}) - 1$, and $f_z(k) \approx 2/k^2$ with $k \ll 1$ in Eqn (8) gives the following result for γ defined by Eqn (7):

$$\gamma \approx 2H_0^2 ab \left(\frac{\pi}{2} - 1 + \frac{1}{2} \ln \frac{4\pi a}{c} \right). \quad (10)$$

The lower inset to Fig. 3 illustrates the comparison of γ values obtained from the general formula (7) and the asymptotic ones fitting Eqn (10).

Let us now consider the influence of a finite crystal length (b dimension) on the γ quantity. Taking a rising additional contribution from ac -faces of the crystal (Fig. 2b) into

account and assuming a tangential distribution of the field component over these faces to be the same as that over the other lateral bc -faces, we obtain from Eqn (7) the following relationship

$$\gamma = 2H_0^2(abf_x + bcf_z + acf_z). \quad (11)$$

However, estimate (11) gives an overestimated value of γ in the case of a real three-dimensional sample. Indeed, the limitation of the crystal length b will result in a decrease in the magnetic field tangential component on the sample surface. The appropriate decrease in γ will not be compensated by the appearance of the $H_t \parallel b$ component which is absent when $b \rightarrow \infty$. Thus, formula (11) represents an upper bound of γ , and its c/a -dependence is shown in the lower inset to Fig. 3.

Experimentally, geometrical factor Γ can be determined in the transverse orientation of the crystal by using a metallic simulator of the tested sample of the same shape and dimensions, provided that the conditions of the normal skin effect are met. Given the simulator resistivity as a function of temperature, $\rho(T)$, and having measured $Q_s(T)$ of the cavity containing the simulator, one can use the relationship $\rho(T) = 2R^2(T)/\omega\mu_0$ and derive the value of Γ from Eqn (2), assuming that it equals the geometrical factor of the HTSC crystal. In order to check the accuracy of the formulas of this section we have measured both the magnetic moment M using ac -susceptibility techniques and geometrical factor γ of superconducting Nb slabs with different a/c and b/a ratios. The discrepancy between theoretical values from Eqn (6) and experimentally obtained values of M reached up to 20% in the case of short ($b \approx 3a$) samples, and decreased to less than 5% for substantially long samples ($b \approx 6a$). In contrast to the magnetic moment, the values of γ proved to be in better agreement with the theory. In fact, divergence has never exceeded 5%, probably due to weaker (logarithmic) dependence of γ on the a/c ratio.

2.3 Electrodynamics of an anisotropic HTSC crystal

The electrodynamics of a layered anisotropic HTSC is characterized by components σ_{ab} and σ_c of the conductivity tensor. In the normal state, the ac field penetrates through a skin depth $\delta_{ab} = \sqrt{2/\omega\mu_0\sigma_{ab}}$ along the c -axis, and through $\delta_c = \sqrt{2/\omega\mu_0\sigma_c}$ in the CuO_2 plane. In the superconducting state, all the parameters δ_{ab} , δ_c , $\sigma_{ab} = \sigma'_{ab} - i\sigma''_{ab}$, and $\sigma_c = \sigma'_c - i\sigma''_c$ are complex. For $T < T_c$, if $\sigma' \ll \sigma''$, the field penetration depths are given by formulas $\lambda_{ab} = \sqrt{1/\omega\mu_0\sigma''_{ab}}$, and $\lambda_c = \sqrt{1/\omega\mu_0\sigma''_c}$. In the close neighborhood of T_c , when $\sigma' \gtrsim \sigma''$, decay of the magnetic field in a superconductor is characterized by functions $\text{Re}(\delta_{ab})$ and $\text{Re}(\delta_c)$, which go over to δ_{ab} and δ_c for $T \geq T_c$, respectively.

In the T-orientation, the surface impedance Z_{ab} is directly connected with the in-plane penetration depth $\lambda_{ab}(T)$ for $T < T_c$, and the skin depth $\delta_{ab}(T)$ for $T \geq T_c$. Both lengths are smaller than the typical crystal thickness. Hence, when the crystal resides in the T-orientation at an arbitrary temperature, the surface impedance Z_{ab} is defined as a coefficient in the Leontovich boundary condition [43], and is correlated with the conductivity σ_{ab} through the local relationship

$$Z_{ab} = R_{ab} + iX_{ab} = \left(\frac{i\omega\mu_0}{\sigma_{ab}} \right)^{1/2}. \quad (12)$$

If the HTSC microwave conductivity is real for $T \geq T_c$, then in the T-orientation the constant f_0 , essential for

determining $X_{ab}(T)$ in Eqn (3), may be found, according to Eqn (12), from the condition that the imaginary and real parts of impedance are equal in the normal state, i.e., as a result of $R_{ab}(T)$ and $\Delta X_{ab}(T)$ coincidence for $T \geq T_c$. It should be pointed out that thermal expansion of the crystal may essentially affect the shape of the $X_{ab}(T)$ curve in the T-orientation. Since the resonance frequency depends on the volume occupied by the field, the crystal expansion is equivalent to a reduction in the magnetic field penetration depth and gives rise to an additional frequency shift $\Delta f_i(T)$ of the cavity [6, 41]:

$$\begin{aligned} \Delta f_i(T) &= \frac{f\mu_0}{8W} \int_s \sum_i \Delta l_i(T) H_t^2 ds \\ &= \frac{f\mu_0 v H_0^2}{4W} (\varepsilon_c f_x + (\varepsilon_a + \varepsilon_b) f_z), \end{aligned} \quad (13)$$

where ε_i is a relative change $\Delta l_i/l_i$ of the sample dimension l_i ($i = a, b, c$), resulting from the thermal expansion, and the functions f_x and f_z are defined according to Eqn (8). In Ref. [41], the contribution (13) to the overall frequency shift is shown to be negligible at low temperatures, however, it becomes noticeable for $T > 0.9 T_c$ in the crystal T-orientation.

In the L-orientation for $T < 0.9 T_c$, the penetration depth in an HTSC crystal is still smaller than the characteristic sample dimensions. It allows us to treat the experimental data in terms of impedance Z_{ab+c} averaged over the sample surface in accordance with Eqn (5). In particular, taking account of the measurements of $\Delta\lambda_{ab}(T) = \Delta X_{ab}(T)/\omega\mu_0$ in the T-orientation and the measured value $\Delta\lambda_{ab+c}(T) = \Delta X_{ab+c}(T)/\omega\mu_0$ in the L-orientation, we obtain

$$\Delta\lambda_c = \frac{(a+c)\Delta\lambda_{ab+c} - a\Delta\lambda_{ab}}{c}. \quad (14)$$

This approach to investigating the impedance anisotropy in HTSC crystals and to determining $\Delta\lambda_c(T)$ was employed in microwave experiments [4, 5, 7, 8 44–47] at low temperatures $T < T_c$. Nevertheless, it does not permit the determination of the value of $\lambda_c(T)$ from the measurements of quality factor and resonance frequency shift in the L-orientation, nor may it be extended to the range of higher temperatures. The point is that the size effect has an essential influence on the L-orientation measurement for $T > 0.9 T_c$, when the penetration depths λ_c and δ_c turn out to be comparable with the crystal width. As a result, the $R_{ab+c}(T)$ temperature dependence measured in the normal state does not coincide with $\Delta X_{ab+c}(T)$, which makes the above-indicated T-orientation method inapplicable to determining f_0 .

In order to analyze the measurement data in the L-orientation in both the superconducting and normal states, we shall avail ourselves of the formulae for field distribution in an anisotropic long strip ($b \gg a, c$) at $\mathbf{H}_\omega \perp \mathbf{c}$ [48]. These formulae neglect the effect of the bc -faces of the crystal, but correctly allow for the size effect. At an arbitrary temperature, the measured quantities ΔQ^{-1} and $\Delta f(T) = \delta f(T) + f_0$ are expressed in terms of a complex function $\mu(T) = \mu'(T) - i\mu''(T)$ [11, 49]:

$$\Delta Q^{-1} - \frac{2i\delta f}{f} = \frac{i\mu_0\mu v H_0^2}{2W}, \quad (15)$$

which is controlled by the components $\sigma_{ab}(T)$ and $\sigma_c(T)$ of the conductivity tensor through the complex penetration

depths δ_{ab} and δ_c :

$$\begin{aligned}\mu &= \frac{8}{\pi^2} \sum_n \frac{1}{n^2} \left(\frac{\tan \alpha_n}{\alpha_n} + \frac{\tan \beta_n}{\beta_n} \right), \\ \alpha_n^2 &= -\frac{a^2}{\delta_c^2} \left(\frac{i}{2} + \frac{\pi^2}{4} \frac{\delta_{ab}^2}{c^2} n^2 \right), \\ \beta_n^2 &= -\frac{c^2}{\delta_{ab}^2} \left(\frac{i}{2} + \frac{\pi^2}{4} \frac{\delta_c^2}{a^2} n^2 \right),\end{aligned}\quad (16)$$

where the summation is taken over odd integers $n > 0$.

If $\sigma' \ll \sigma''$ in the superconducting state, we get

$$\begin{aligned}\mu' &\approx \frac{8}{\pi^2} \sum_n \frac{1}{n^2} \left(\frac{\tanh \tilde{\alpha}_n}{\tilde{\alpha}_n} + \frac{\tanh \tilde{\beta}_n}{\tilde{\beta}_n} \right), \\ \tilde{\alpha}_n^2 &= \frac{a^2}{\lambda_c^2} \left(\frac{1}{4} + \frac{\pi^2}{4} \frac{\lambda_{ab}^2}{c^2} n^2 \right), \\ \tilde{\beta}_n^2 &= \frac{c^2}{\lambda_{ab}^2} \left(\frac{1}{4} + \frac{\pi^2}{4} \frac{\lambda_c^2}{a^2} n^2 \right).\end{aligned}\quad (17)$$

In particular, $\lambda_{ab} \ll c$ and $\lambda_c \ll a$ for $T < 0.9 T_c$, so we derive a simple expression for the real part of μ from Eqn (17):

$$\mu' = \frac{2\lambda_c}{a} + \frac{2\lambda_{ab}}{c}. \quad (18)$$

One can easily verify that in the range of low temperatures the change in $\Delta\lambda_c(T)$ prescribed by Eqn (18) is identical to that in Eqn (14).

In the normal state, the conductivity $\sigma' \gg \sigma''$. If the sample dimensions were much more than the penetration depths, we would obtain the following relations from Eqns (15), (16):

$$\Delta Q^{-1} - 2i \frac{\delta f}{f} \approx \frac{\mu_0 v H_0^2}{2W} (1+i) \left(\frac{\delta_c}{a} + \frac{\delta_{ab}}{c} \right), \quad (19)$$

i.e., the temperature dependences of $\Delta(1/Q)$ and $(-2\delta f/f)$ would be identical for $T > T_c$, and the values $R_{ab+c}(T)$ and $X_{ab+c}(T)$, derived from Eqns (2)–(5), would be equal. In practice, the value of $\delta_c \sim 0.1$ mm ($f \sim 10$ GHz) proves to be comparable with the crystal width a even for YBCO crystals which can be referred to as weakly anisotropic in comparison with other layered HTSCs. So, to determine the surface impedance components from the measurements in the crystal L-orientation, it is necessary to apply the general formulae (15) and (16), as will be shown in Section 2.4.

Thus, in Sections 2.2 and 2.3, the electrodynamic technique developed in Refs [6, 11, 41, 48, 49] was analyzed as to the determination of the components of the surface impedance and complex conductivity tensors of HTSC single crystals on the basis of measured quantities of a quality factor and a resonator frequency shift. Expression (7) was obtained for a geometrical factor of a crystal in the form of a plane-parallel plate with dimensions $b \gg a > c$ in a microwave magnetic field $\mathbf{H}_\omega \parallel c$. Given Γ , from Eqns (2) and (3) we find the impedance Z_{ab} and, according to Eqn (12), the conductivity $\sigma_{ab}(T) = i\omega\mu_0/Z_{ab}^2(T)$ in the T-orientation of the sample. To obtain the c -axis components of complex conductivity and surface impedance from measurements in the L-orientation ($\mathbf{H}_\omega \perp c$), a procedure which takes account of the sample size effects was proposed. Together, these results allow one to get the complex conductivity tensor with high accuracy in both the normal and superconducting states,

and provide the electrodynamic basis for the anisotropy measurements in HTSC crystals.

2.4 Impedance and conductivity of YBa₂Cu₃O_{6.93} single crystal

Let us employ the formulae given in Sections 2.1–2.3 for determining the temperature dependences of all components of the impedance and conductivity tensors of an optimally doped YBa₂Cu₃O_{6.93} single crystal in its normal and superconducting states. The crystal was grown using the method of slow cooling from a solution–melt with the use of a BaZrO₃ crucible [6, 50]. The crystal represented a prolate parallelepiped with the dimensions $a \times b \times c = 0.4 \times 1.6 \times 0.1$ mm³. The sample geometrical factor calculated from Eqns (4) and (7) equaled $\Gamma = 90$ kΩ. The surface impedance was measured at a frequency of $f = 9.42$ GHz in the T- and L-orientations (Fig. 2).

Figure 4 displays the temperature dependences of $R_{ab}(T)$ and $X_{ab}(T)$ components in the normal and superconducting states of the crystal, measured in the T-orientation. The upper inset to this figure displays the measured temperature dependences of ΔQ^{-1} (squares) and $-2\Delta f/f$ (triangles) in the normal state of the crystal. The curves $\Delta Q^{-1}(T)$ and $-2\delta f(T)/f = -2(\Delta f(T) + \Delta f_i(T) + f_0)/f$ (circles) are superimposed when taking into account the additional frequency shift $\Delta f_i(T)$ from Eqn (13), which arises due to the sample thermal expansion [41, 51], along with the constant f_0 which is independent of temperature. The coincidence of $\Delta Q^{-1}(T)$ and $-2\delta f(T)/f$ curves and, therefore, the equality $R_{ab}(T) = X_{ab}(T)$ emerging from Eqns (2) and (3) for $T > T_c$, demonstrate the fulfilling of the normal skin-effect condition in the ab -planes of YBa₂Cu₃O_{6.93} single crystals in the T-orientation. A linear temperature dependence of the resistivity $\rho_{ab}(T) = 1/\sigma_{ab}(T) = 0.63 T \mu\Omega$ cm within the range $100 \leq T < 200$ K together with the skin depth $\delta_{ab}(150 \text{ K}) = 5 \mu\text{m}$ are derived from formula (12).

In the superconducting state, the dependence $R_{ab}(T)$ has a broad peak in the vicinity of $T \sim T_c/2$, characteristic of optimally doped YBCO crystals. The dependences $R_{ab}(T)$ and $\lambda_{ab}(T) = X_{ab}(T)/\omega\mu_0$ are linear for $T < T_c/3$ (see lower

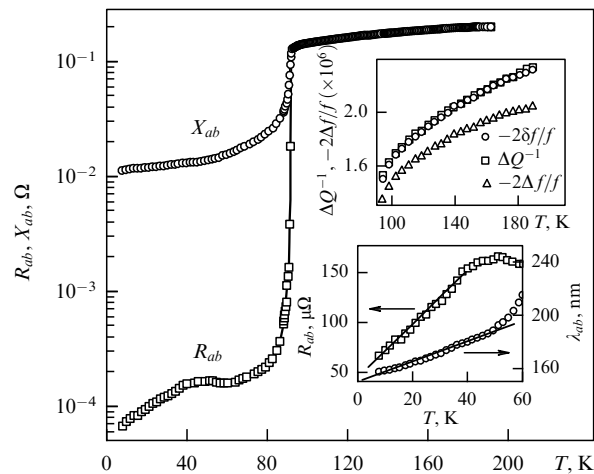


Figure 4. $R_{ab}(T)$ and $X_{ab}(T)$ dependences for a YBa₂Cu₃O_{6.93} single crystal (T-orientation). The upper inset shows the measured temperature dependences $-2\Delta f/f$ (triangles) and ΔQ^{-1} (squares). Taking the constant f_0 and thermal expansion into account we get $-2\delta f/f$ (circles). The lower inset displays $R_{ab}(T)$ and $\lambda_{ab}(T)$ dependences at low T .

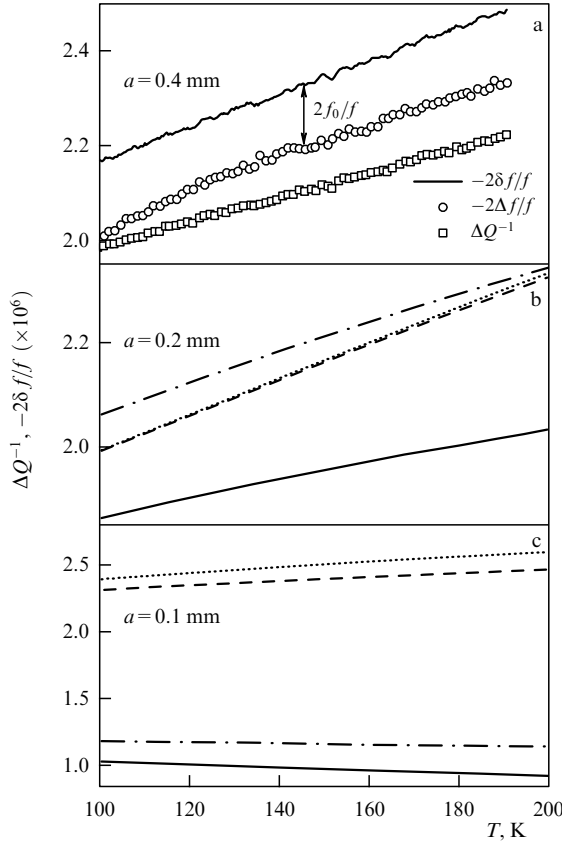


Figure 5. (a) ΔQ^{-1} (squares) and $-2\Delta f/f$ (circles) dependences measured in the L-orientation of a $\text{YBa}_2\text{Cu}_3\text{O}_{6.93}$ single crystal for $T \geq 100$ K. The solid line shows the temperature dependence of $-2\delta f/f$ derived from Eqns (15) and (16). The constant $2f_0/f$ is indicated by the arrow. (b) ΔQ^{-1} and $-2\delta f/f$ dependences calculated from Eqns (15) and (16) (solid and dashed lines, respectively) and from Eqns (20) and (21) (dot-and-dash and dotted lines, respectively) for a sample width $a = 0.2$ mm. (c) The same as in figure (b) but for $a = 0.1$ mm.

inset to Fig. 4). Their extrapolation to zero temperature yields the values of the residual surface resistance $R_{ab}(0) \approx 40 \mu\Omega$ and penetration depth $\lambda_{ab}(0) \approx 150$ nm into the cuprate planes of the sample.

Equations (15) and (16) are used to analyze the experimental data for the L-orientation of the crystal. The real part of formula (15) defines the relation between $\Delta Q^{-1}(T)$ and $\delta_{ab}(T)$ and $\delta_c(T)$. Upon measuring the dependence $\Delta Q^{-1}(T)$ (squares in Fig. 5a) for $T > T_c$ in the L-orientation and taking the dependence $\delta_{ab}(T) = \sqrt{2\rho_{ab}(T)/\omega\mu_0}$ measured in the T-orientation into account, we obtain from Eqn (16) the function $\delta_c(T) = \sqrt{2\rho_c(T)/\omega\mu_0}$, with $\delta_c(150 \text{ K}) = 0.06$ mm, and the dependence $\rho_c(T) = 10^4 + 24 T \mu\Omega \text{ cm}$ in the range $100 \leq T < 200$ K. Using already determined dependences $\delta_c(T)$ and $\delta_{ab}(T)$ and having computed the real part $\mu'(T)$ in Eqn (16), from Eqn (15) we calculate $(-2\delta f/f)$ versus temperature for $T > T_c$, the result being shown by the solid line in Fig. 5a. This line is approximately parallel to the experimental curve $-2\Delta f(T)/f$ in the L-orientation (circles in Fig. 5a) for $T > 110$ K. The difference $-2(\delta f - \Delta f)/f$ yields the additive constant f_0 . Given f_0 and $\Delta f(T)$, we obtain $\delta f(T)$ over the temperature range $5 < T < 200$ K in the L-orientation.

It should be emphasized that the discrepancy between the curves $\Delta Q^{-1}(T)$ and $-2\delta f(T)/f$ for $T > T_c$ in the

L-orientation does not originate from the thermal expansion of the crystal essential in the T-orientation, but arises due to the size effect. This discrepancy becomes more noticeable with a decrease in the crystal width a , when it becomes equal to the skin depth δ_c . The results computed for $\Delta Q^{-1}(T)$ (solid line) and $-2\delta f(T)/f$ (dashed line) from Eqns (15) and (16) using the above-mentioned dependences $\rho_{ab}(T)$ and $\rho_c(T)$ are shown in Figs 5b and 5c for $a = 0.2$ mm and $a = 0.1$ mm.

It should be noticed that due to the size effect in anisotropic HTSC crystals for $T > 0.9 T_c$, the surface impedance components R_{ab+c} and X_{ab+c} in Eqn (5) cannot be found from the values of ΔQ^{-1} and $\delta f/f$ measured in the L-orientation with the use of formulae (2) and (3). Moreover, it is also incorrect to replace the values of R and X in these formulae by their effective values $R^{\text{eff}}(d)$ and $X^{\text{eff}}(d)$ for a thin metal plate of width $d \sim \delta$, placed in the field \mathbf{H}_ω parallel to its infinite surfaces:

$$R^{\text{eff}}(d) = R \frac{\sinh \eta - \sin \eta}{\cosh \eta + \cos \eta},$$

$$X^{\text{eff}}(d) = R \frac{\sinh \eta + \sin \eta}{\cosh \eta + \cos \eta}, \quad (20)$$

where $\eta = \omega\mu_0 d/2R$, and $R = \sqrt{\omega\mu_0\rho/2}$. The point is that though allowing the usage of formulae (20) in Eqns (2), (3), and (5) in the event $d \sim \delta$, the solution of Maxwell equations yields an incorrect (one-dimensional) distribution of high-frequency currents in the normal state of an anisotropic crystal. Indeed, for a plate of width a and thickness c , elongated along the edge $b \parallel \mathbf{H}_\omega$, we obtain from Eqns (2)–(5) the relationship

$$\Delta Q^{-1} - \frac{2i\delta f}{f} = \frac{H_0^2}{\omega W} [abZ_{ab}^{\text{eff}}(c) + bcZ_c^{\text{eff}}(a)], \quad (21)$$

where the effective values $Z_{ab}^{\text{eff}}(c) = R_{ab}^{\text{eff}}(c) + iX_{ab}^{\text{eff}}(c)$ and $Z_c^{\text{eff}}(a) = R_c^{\text{eff}}(a) + iX_c^{\text{eff}}(a)$ are found from Eqn (20). Figures 5b) and 5c) display the result calculated for $\Delta Q^{-1}(T)$ and $-2\delta f(T)/f$ from Eqns (20) and (21), and above-determined dependences $\rho_{ab}(T)$ and $\rho_c(T)$ in the case of two plates: the first plate of dimensions $a \times b \times c = 0.2 \times 1.6 \times 0.1 \text{ mm}^3$, and the second with the same values of b and c but half the width $a = 0.1$ mm. Presently, having compared these results with the ones obtained from Eqns (15) and (16), we can see that the approximation (21) at $a \approx 3\delta_c$ (two upper straight lines in Fig. 5b) proves to be practically insensitive to the size effect, giving rise to weakly differing dependences $\Delta Q^{-1}(T)$ and $-2\delta f(T)/f$ for $T > 100$ K. Only in the case of the crystal width $a = 0.1$ mm ($a \sim \delta_c$) does approximation (21) lead to the result portrayed in Fig. 5c, resembling the one obtained with the aid of the general formulae (15) and (16).

Upon finding the dependences $\Delta Q^{-1}(T)$, $\delta f(T)$ and, hence, the function $\mu(T)$ entering Eqn (15) in the normal and superconducting states of $\text{YBa}_2\text{Cu}_3\text{O}_{6.93}$ crystal in the L-orientation and using the temperature dependences of conductivities σ'_{ab} and σ''_{ab} (see Fig. 6) found from Eqn (12), we get the c -axis conductivity components $\sigma'_c(T)$ and $\sigma''_c(T)$ from Eqn (16), which are shown in Fig. 6.

In the case of a local coupling between the electric field and the current along the c -axis, the surface impedance $Z_c(T) = R_c(T) + iX_c(T)$ is related to the conductivity $\sigma_c(T) = \sigma'_c(T) - i\sigma''_c(T)$ through the expres-

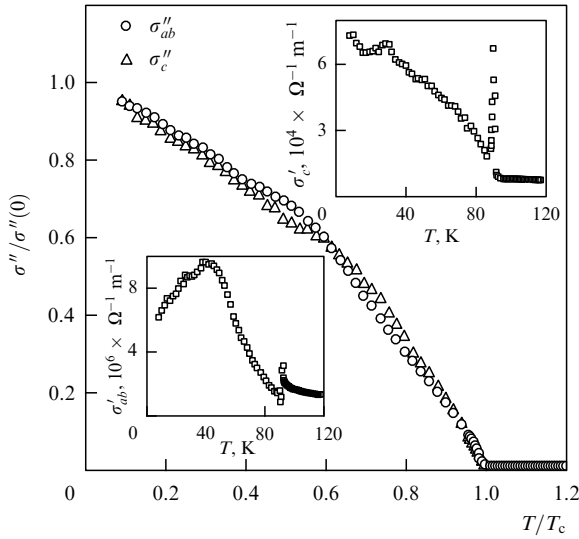


Figure 6. The conductivities $\sigma''_{ab}/\sigma''_{ab}(0)$ and $\sigma''_c/\sigma''_c(0)$ of $\text{YBa}_2\text{Cu}_3\text{O}_{6.93}$ single crystal versus T/T_c . The insets display $\sigma'_{ab}(T)$ and $\sigma'_c(T)$ dependences.

sion $\sigma_c(T) = i\omega\mu_0/Z_c^2(T)$. Figure 7 displays the components of $Z_c(T)$, obtained in this manner. In the insets to Fig. 7, the $R_c(T)$ and $\lambda_c(T) = X_c(T)/\omega\mu_0$ dependences for $T < T_c/2$ demonstrate linear behavior. Extrapolated to $T = 0$ K, the value of the penetration depth along cuprate planes of $\text{YBa}_2\text{Cu}_3\text{O}_{6.93}$ single crystal is equal to $\lambda_c(0) \approx 1.55 \mu\text{m}$.

From Eqn (5) one can easily estimate that in the L-orientation of our crystal the contribution of the c -axis currents to measurable quantities is about two times greater than that of the ab -plane ones: $bcZ_c \approx 2abZ_{ab}$. Taking the accuracy of determination of $R_{ab}(T)$ ($< 5\%$) and $\Delta\lambda_{ab}(T)$ (a few angstroms) values into account, we conclude that the linear behavior of $R_c(T)$ and $\lambda_c(T)$ at low temperatures is a property of optimally doped $\text{YBa}_2\text{Cu}_3\text{O}_{6.93}$ and is not due to the inaccuracy of the method employed. The linear temperature dependence of λ_c for $T < T_c/2$ is also confirmed by the previous microwave [4, 5] and low-frequency [52] measurements in $\text{YBa}_2\text{Cu}_3\text{O}_{6.93}$. In contrast to the authors of Ref. [7], we did not observe a rise in $R_c(T)$ at low temperatures. Our $R_c(T)$ measurements are in agreement with the ones taken in Refs [4, 45].

2.5 Impedance anisotropy of $\text{YBa}_2\text{Cu}_3\text{O}_{7-x}$ at varying x

To change the oxygen content in the initial $\text{YBa}_2\text{Cu}_3\text{O}_{6.93}$ crystal, we controllably annealed the sample in atmospheric

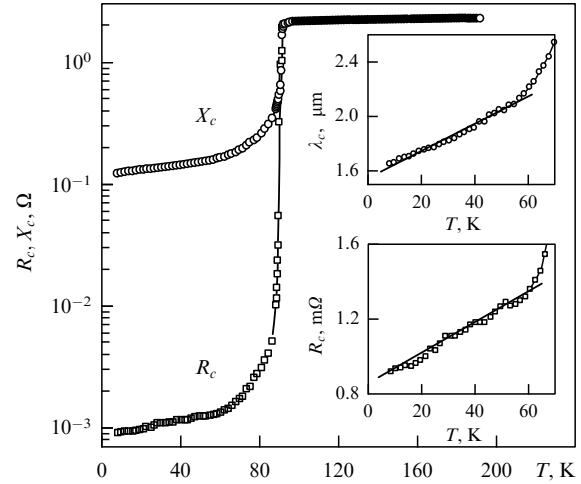


Figure 7. $R_c(T)$ and $X_c(T)$ dependences of $\text{YBa}_2\text{Cu}_3\text{O}_{6.93}$ single crystal. The insets demonstrate $R_c(T)$ and $\lambda_c(T)$ at low temperatures.

air during the two days at different temperatures $T \geq 500^\circ\text{C}$, specified in Table 1, and then quenched it with liquid nitrogen. Measurements of the conductivity anisotropy were carried out at temperatures $5 \leq T \leq 200$ K in Ref. [53] for each of the five crystal states in which the superconducting transition width, according to susceptibility measurements at a frequency of 100 kHz, amounted to 0.1 K in the optimally doped ($x = 0.07$) state and increased with x , having reached 4 K at $x = 0.47$. The superconducting transition temperatures were $T_c = 92, 80, 70, 57$, and 41 K. Using the empirical relationship [54] $T_c = T_{c,\text{max}}[1 - 82.6(p - 0.16)^2]$ with $T_{c,\text{max}} = 92$ K at $p = 0.16$ ($x = 0.07$), we got the hole concentrations $p = 0.12, 0.106, 0.092$, and 0.078 per copper atom in the CuO_2 plane for the four other states of $\text{YBa}_2\text{Cu}_3\text{O}_{7-x}$ with lower T_c values and $x = 0.26, 0.33, 0.40$, and 0.47, respectively. As before, the whole cycle of measurements included the following steps: (i) we measured the temperature dependences of the quality factor and the frequency shift of the superconducting niobium cavity with the sample resided in two, transverse and longitudinal, orientations about the microwave magnetic field; (ii) determination of the surface resistance $R_{ab}(T)$, reactance $X_{ab}(T)$, and conductivity $\sigma_{ab}(T)$ of the crystal cuprate planes in the normal and superconducting states from the measurements in the first orientation, and (iii) determination of $\sigma_c(T)$, $X_c(T)$, and $R_c(T)$ using the data obtained for both orientations.

The temperature dependences of surface impedance components in the ab -plane and along the c -axis are shown

Table 1. Annealing and critical temperatures, doping parameters, characteristics of the microwave ab -plane response*, and field penetration depths in $\text{YBa}_2\text{Cu}_3\text{O}_{7-x}$ crystal.

Annealing temperature T , $^\circ\text{C}$	Critical temperature T_c , K	Doping parameters		ab -plane characteristics				λ values at $T = 0$		$\Delta\lambda_c(T) \propto T^\alpha$	λ_c/λ_{ab} at $T = 0$
		p	x	δT_c , K	R_{res} , $\mu\Omega$	$\tau_{ab}(T_c) \times 10^{13}$, s	β	λ_{ab} , nm	λ_c , μm		
500	92	0.16	0.07	0.5	55	0.7	0.05	152	1.55	1.0	10
520	80	0.12	0.26	1	54	0.9	0.06	170	3.0	1.1	18
550	70	0.106	0.33	1.5	50	1.0	0.10	178	5.2	1.2	29
600	57	0.092	0.40	1.5	35	1.4	0.13	190	6.9	1.3	36
720	41	0.078	0.47	4.0	30	1.5	0.20	198	16.3	1.8	83

* transition width δT_c , residual surface resistance R_{res} , relaxation time $\tau_{ab}(T_c)$, and parameter $\beta \approx \tau_{ab}(T_c)/\tau_{ab}(0)$.

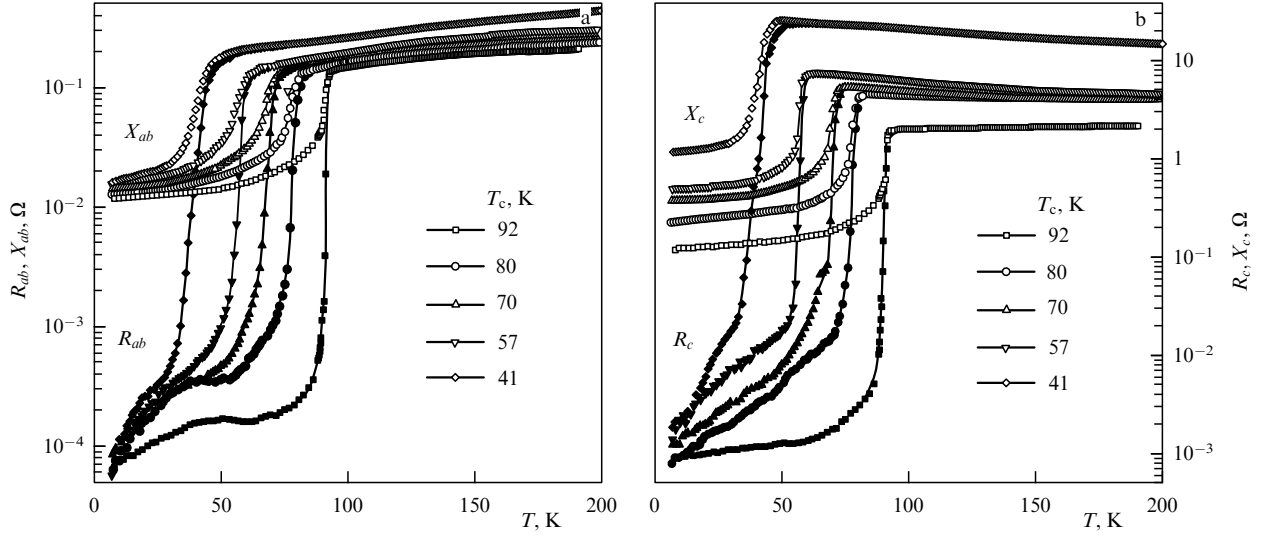


Figure 8. (a) Real $R_{ab}(T)$ (full symbols) and imaginary $X_{ab}(T)$ (open symbols) parts of the ab -plane surface impedance for the five states of $\text{YBa}_2\text{Cu}_3\text{O}_{7-x}$ single crystal, and (b) the components of the c -axis surface impedance.

in Fig. 8 for each of the five crystal states indicated in Table 1. In Sections 3–5 we will discuss at length these curves for the normal and superconducting states of the crystal.

3. Normal state

3.1 Normal skin effect

Whereas the conditions $R_{ab}(T) = X_{ab}(T)$ for $T \gtrsim T_c$ and $\Delta X_{ab}(T) < \Delta R_{ab}(T)$ for $T \lesssim T_c$ were experimentally examined for YBCO [20, 45, 55–57], BSCCO [8, 11, 55, 57], TBCCO [12], BaKBiO [37], and LaSrCuO [58], the reactance variation $\Delta X_{ab}(T)$ in crystals TBCO [14, 15, 59], HgBaCuO, and HgBaCaCuO [59] is considerably larger than that of the resistance $\Delta R_{ab}(T)$ within the entire temperature range, so that $R_{ab}(T) \neq X_{ab}(T)$ for $T \gtrsim T_c$. In Ref. [59], this breaking of the normal skin-effect condition was treated in terms of a collective phason mode. In model [60], the appearance of the inequality $R_{ab}(T) \neq X_{ab}(T)$ was due to the presence of superconducting islands embedded in a normal metallic matrix. Both concepts are related to the pseudogap phenomenon in HTSCs. As an alternative explanation, we proposed in Ref. [61] that the shielding effect of the microwave magnetic field by the roughnesses of TBCO crystal, formed by cleavage plane traces on its surface, should be allowed for. If the field penetration depth is much less than the surface roughness, both components of the effective (i.e., measured) surface impedance will increase in comparison with their values for a flat surface by the same factor equal to the ratio of the real and flat surface areas. If the roughness sizes are comparable to the penetration depth, a situation may occur where the microwave magnetic field \mathbf{H}_ω is slightly distorted by the roughness, whereas the high-frequency current \mathbf{j}_ω caused by the field decays noticeably [62]. In this case, the effective reactance ($\sim \omega \mu_0 \int H_\omega^2 dV$) will exceed the sample surface resistance ($\sim \int \mathbf{j}_\omega^* E_\omega dV$). It is likely that this is the case for a TBCO crystal whose surface roughnesses proved to be comparable with its skin depth ($\sim 5 \mu\text{m}$ at a frequency of $\approx 10 \text{ GHz}$). Indeed, scanning electron micrographs of the TBCO crystal surface demonstrated [15] that traces of the cleavage planes form juts (grooves) in the form of parallel

channels at the surface, and the extent (height, width, spacing) of the roughnesses is about $1 \mu\text{m}$.

3.2 Resistivity of the cuprate planes

As follows from Fig. 8, the real and imaginary parts of the surface impedance coincide at every x in the normal state (for $T > T_c$) of $\text{YBa}_2\text{Cu}_3\text{O}_{7-x}$ crystal: $R_{ab}(T) = X_{ab}(T)$, and $R_c(T) = X_c(T)$. Therefore, the resistivities $\rho_{ab}(T)$ and $\rho_c(T)$ were found from $R_{ab}(T)$ and $R_c(T)$ curves, applying the standard formulas of the normal skin effect: $\rho_{ab}(T) = 2R_{ab}^2(T)/\omega\mu_0$, and $\rho_c(T) = 2R_c^2(T)/\omega\mu_0$. Figure 9 portrays the evolution of the dependences $\rho_{ab}(T)$ and $\rho_c(T)$ with the variation in x within the temperature range $T_c < T \leq 200 \text{ K}$.

The ab -plane transport in the normal state of $\text{YBa}_2\text{Cu}_3\text{O}_{7-x}$ crystal always remains metallic: the derivatives of $\rho_{ab}(T)$ with respect to temperature are positive. The low value of $\rho_{ab}(T_c) \lesssim 50 \mu\Omega \text{ cm}$ is indicative of the high quality of the crystal. As in a normal metal, the resistivity in the ab -planes of optimally doped HTSCs increases proportionally to temperature due to an electron–phonon interaction: $\Delta\rho_{ab}(T) \propto 1/\tau_{ab}(T) \propto T$, where τ_{ab} is the quasiparticle relaxation time in the cuprate planes. The low-frequency conductivity of these planes can be considered as a Drude one:

$$\sigma_{ab} = \frac{n_{2D} e^2 \tau_{ab}}{md}, \quad (22)$$

where $n_{2D} = k_F^2/2\pi$ is the 2D quasiparticle density.

Notice that the weak inflections are seen in the two lower $\rho_{ab}(T)$ curves in Fig. 9 around $T \sim 100 \text{ K}$. As will be shown in Section 5.1, these inflections are accompanied by distinctions in the $\Delta\lambda_{ab}^{-2}(T)$ curves for $\text{YBa}_2\text{Cu}_3\text{O}_{6.60}$ and $\text{YBa}_2\text{Cu}_3\text{O}_{6.53}$ in the superconducting state of these samples.

3.3 The c -axis resistivity

As follows from Fig. 9, only the optimally doped $\text{YBa}_2\text{Cu}_3\text{O}_{6.93}$ exhibits that both dependences $\rho_{ab}(T)$ and $\rho_c(T)$ possess metallic behavior. The other states of $\text{YBa}_2\text{Cu}_3\text{O}_{7-x}$ with lower concentrations of holes have the

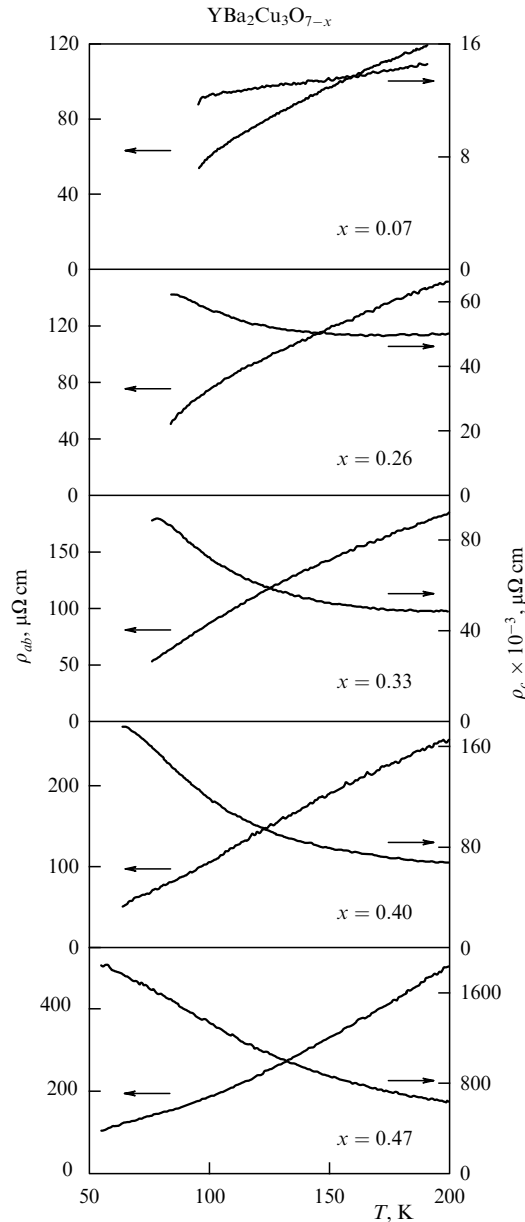


Figure 9. The evolution of the measured $\rho_{ab}(T)$ and $\rho_c(T)$ dependences in $\text{YBa}_2\text{Cu}_3\text{O}_{7-x}$ with varying oxygen content.

resistivity $\rho_c(T)$ increasing with decreasing temperature, thus exhibiting nonmetallic behavior. Figure 10 represents the experimental dependences $\sigma_c(T)$ compared to the values of $\sigma_{c,\min}^{3D}$, calculated using formula (1) for the three states of the $\text{YBa}_2\text{Cu}_3\text{O}_{7-x}$ crystal with $T_c = 92$ K (dashed line), $T_c = 70$ K (dotted line), and $T_c = 41$ K (dot-and-dash line). It is only the c -axis conductivity of $\text{YBa}_2\text{Cu}_3\text{O}_{6.93}$ that exceeds the minimum metallic value of $\sigma_{c,\min}^{3D}$ in the whole temperature range.

Thus, it is natural to assume that a slight decrease in the carrier concentration p (in comparison with the optimal level $p = 0.16$) in the normal state of $\text{YBa}_2\text{Cu}_3\text{O}_{7-x}$ results in the crossover from 3D metallic conductivity at $x = 0.07$ to 2D Drude conductivity in CuO_2 layers and tunneling conductivity [63–67] between these layers for $x > 0.07$ (the 3D–2D crossover). It happens when the interplane hopping time becomes comparable to the in-plane scattering time τ_{ab} . In Refs [68, 69], a criterion for the 3D–2D transition was

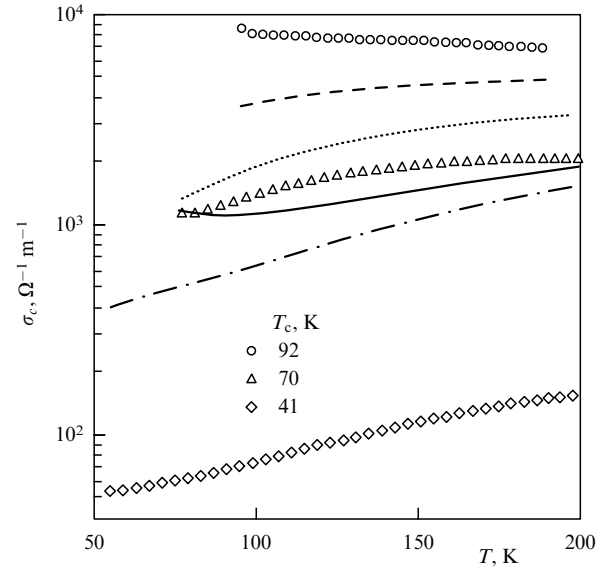


Figure 10. The symbols portray experimental dependences for the $\sigma_c(T)$ in three states of $\text{YBa}_2\text{Cu}_3\text{O}_{7-x}$ at $T_c = 92$ K, $T_c = 70$ K, and $T_c = 41$ K. The dashed, dotted, and dash-dot lines trace the values of $\sigma_{c,\min}^{3D}(T)$ corresponding to these states and obtained from formula (1) using the measured $\rho_{ab}(T)$ and $\rho_c(T)$ in Fig. 9. The solid line represents calculation of $\sigma_c(T)$ for $\text{YBa}_2\text{Cu}_3\text{O}_{6.67}$, using the formulae from Ref. [63].

obtained, namely

$$\sigma_{c,\max}\sigma_{ab} \approx \frac{n_{2D}}{\pi} \left(\frac{e^2}{h} \right)^2, \quad (23)$$

where σ_{ab} is given by formula (22), and $\sigma_{c,\max}$ is the maximal value of tunneling c -axis conductivity $\sigma_{c,\max} \approx \sigma_{\text{IR}} \sqrt{\rho_{ab}/\rho_c}$, which is approximately equal to the minimal metallic conductivity $\sigma_{c,\min}^{3D}$ from Eqn (1). At $n_{2D} = n/d \approx 10^{14} \text{ cm}^{-2}$ in HTSCs, formula (23) demonstrates that the 3D–2D crossover sets in when the value of $\rho_c \rho_{ab} \approx 10^{-6} \Omega^2 \text{ cm}^2$ is reached. The data in Fig. 9 give $\rho_c \rho_{ab} \lesssim 10^{-6} \Omega^2 \text{ cm}^2$ at $x = 0.07$ only, which confirms that the 3D anisotropic Fermi-liquid model is applicable for explaining the transport properties of the optimally doped $\text{YBa}_2\text{Cu}_3\text{O}_{6.93}$ crystal.

The approximate temperature dependence obtained in Ref. [63] for the c -axis conductivity $\sigma_c(T) \propto (A/T + C + BT)$, where A, B, C are temperature independent, does not fit experimental data; the solid line in Fig. 10 represents an example of the calculation of $\sigma_c(T)$ using the formulae from Ref. [63] for $\text{YBa}_2\text{Cu}_3\text{O}_{6.67}$. However, recently another c -transport model was proposed in Ref. [70], well describing all the dependences $\rho_c(T)$ shown in Fig. 9. Unlike the papers [63], where the interaction effects with phonons show themselves in the second order of the perturbation theory, the Hamiltonian in the model [70] allows for these effects accurately through a canonical transformation [71]; only later is this interplanar tunneling of quasiparticles considered as a perturbation of an electron–phonon system which is strongly coupled initially. Such a consideration is applicable if $\varepsilon_F \gg \omega_0 \gg t_\perp$, where ε_F is the Fermi energy, ω_0 is a typical phonon energy, and t_\perp is an interplane hopping matrix element. Both inequalities hold for layered anisotropic HTSCs, where, according to Ref. [70], an electron moving in the c -direction is surrounded by a large number of phonons forming a polaron [72] which influences the transversal ab -transport weakly. The following analytic expression was obtained in Ref. [70] for the Einsteinian spectrum of

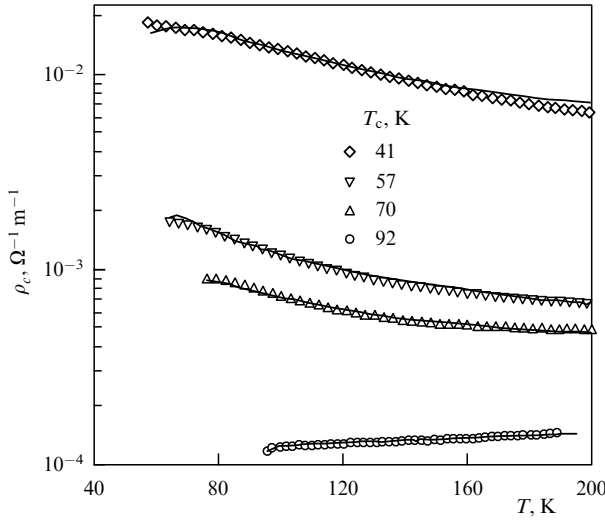


Figure 11. Comparison of the experimental $\rho_c(T)$ dependences in $\text{YBa}_2\text{Cu}_3\text{O}_{7-x}$ (symbols) and those calculated from Eqn (24) (solid lines).

c -polarized phonons in the temperature range around $T \sim \omega_0$:

$$\rho_c(T) \propto \rho_{ab}(T) \frac{\exp[g^2 \tanh(\omega_0/4T)]}{\sqrt{\sinh(\omega_0/2T)}}, \quad (24)$$

where g is a parameter characterizing the strength of electron–phonon interaction ($g > 1$). Figure 11 compares our experimental $\rho_c(T)$ dependences (symbols) and those calculated from Eqn (24) (solid lines). To calculate there, we used the $\rho_{ab}(T)$ data from Fig. 9; g was almost the same for all the dependences in Fig. 11 ($g \approx 3$); ω_0 increased from an equivalent temperature of 110 K (75 cm^{-1}) to 310 K (215 cm^{-1}) when the oxygen content ($7-x$) was decreased in $\text{YBa}_2\text{Cu}_3\text{O}_{7-x}$ from 6.93 to 6.53.

Thus, an analysis of the temperature dependences of the resistivity $\hat{\rho}(T)$ tensor in the normal state revealed that the optimally doped $\text{YBa}_2\text{Cu}_3\text{O}_{6.93}$ is a three-dimensional anisotropic metal. A decrease in its hole concentration p results in the crossover from Drude c -axis conductivity to the hopping one. It appears when the value of $\rho_c \rho_{ab} \approx 10^{-6} \Omega^2 \text{ cm}^2$ is reached. In order to quantitatively describe the evolution of the $\rho_c(T)$ dependences at varying p , it is necessary to allow for the effects of strong electron–phonon interaction in the cuprate planes.

4. Superconducting state

4.1 Surface impedance

Figure 12 depicts the low-temperature sections of the measured $\lambda_{ab}(T) = X_{ab}(T)/\omega\mu_0$ curves for five states of $\text{YBa}_2\text{Cu}_3\text{O}_{7-x}$ crystal. The linear extrapolation (dashed lines) of these dependences for $T < T_c/3$ to $T \rightarrow 0$ gives the $\lambda_{ab}(0)$ values listed in Table 1. The error in the absolute value of $\lambda_{ab}(0)$ is mainly governed by the accuracy in the determination of the additive constant f_0 in Eqn (3). In our experiments, the root-mean-square difference between $R_{ab}(T)$ and $X_{ab}(T)$ in the normal state of the crystal corresponded to about 5-nm uncertainty in the $\lambda_{ab}(0)$ value.

In $\text{YBa}_2\text{Cu}_3\text{O}_{6.93}$ ($p = 0.16$), the temperature dependence of $R_{ab}(T)$ in Fig. 4 has a broad peak in the vicinity of $T \sim T_c/2$, which is characteristic for high-quality optimally

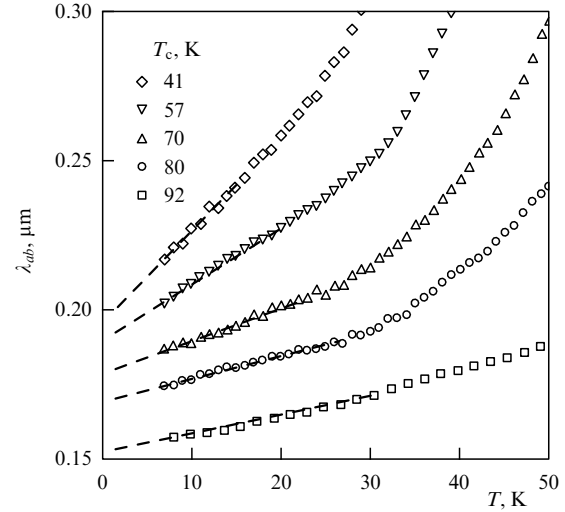


Figure 12. Low-temperature $\lambda_{ab}(T)$ dependences (symbols) measured for five states of $\text{YBa}_2\text{Cu}_3\text{O}_{7-x}$ crystal with $T_c = 92 \text{ K}$, $T_c = 80 \text{ K}$, $T_c = 70 \text{ K}$, $T_c = 57 \text{ K}$, and $T_c = 41 \text{ K}$. Dashed lines are the linear extrapolations for $T < T_c/3$.

doped YBCO crystals. The peak is gradually smeared when p is lowered (Fig. 8a). Note that such a peak has not been observed in any BSCCO (Fig. 13), TBCCO, TBCO, and LaSrCuO crystals with tetragonal or cubic (BaKBiO) lattices.

In Table 2, we summarize the main peculiarities of the temperature dependences of the ab -plane surface impedance in optimally doped YBCO, BSCCO, TBCO, and TBCCO single crystals at the frequencies $\approx 10 \text{ GHz}$. The common features of all these materials are the linear temperature dependences of the surface resistance $\Delta R_{ab}(T) \propto T$ and reactance $\Delta X_{ab}(T) \propto \Delta \lambda_{ab}(T) \propto T$ as $T \ll T_c$. The region of linear resistance extends to near $T_c/2$ for the tetragonal crystals (lower inset to Fig. 13) and terminates near or below $T = T_c/3$ for YBCO (lower inset to Fig. 4). In addition, the

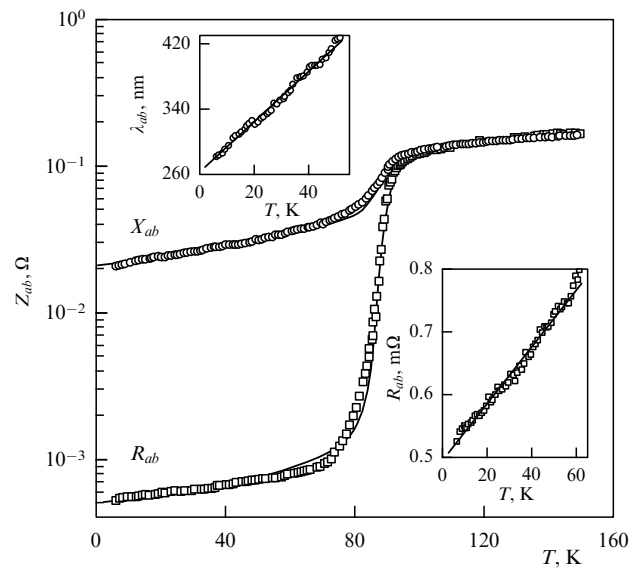


Figure 13. Surface resistance $R_{ab}(T)$ and reactance $X_{ab}(T)$ in the ab -plane of optimally doped BSCCO single crystal [11]. The solid curves are the T -dependences of the surface impedance components calculated using the modified two-fluid model (see Section 4.3). The insets show linear sections of $\lambda_{ab}(T)$ and $R_{ab}(T)$ curves at low temperatures.

Table 2. Surface resistance $R_{ab}(T)$, reactance $X_{ab}(T)$, penetration depth $\lambda_{ab}(T)$, resistivity $\rho_{ab}(T)$, and their changes with temperature T in the ab -plane of high- T_c optimally doped single crystals at frequencies ~ 10 GHz.

HTSC	Superconducting state, $T < T_c$			Normal state, $2T_c > T \geq T_c$
	Low temperatures, $2 \text{ K} < T \ll T_c$	Intermediate temperatures, $T \sim T_c/2$	$T \rightarrow T_c$	
Orthorhombic YBCO structure, $T_c \approx 92 \text{ K}$	$\Delta R(T) \propto T, \Delta X(T) \propto T$ for $T \lesssim T_c/4$; different slopes of $\Delta \lambda(T) \propto T$ [18–24]	Broad peak in $R(T)$ for $25 < T < 45 \text{ K}$ [3–7, 15–24]. Peculiarities: 1) shoulder [21, 22] in $R(T)$ for $T > 40 \text{ K}$; 2) bump [21] or plateau [20] in the $X(T)$ curves for $50 < T < 80 \text{ K}$	Different slopes of $\lambda(T)$ [18–24]	Normal skin effect $R(T) = X(T) = \sqrt{\omega \mu_0 \rho(T)/2}$, $\Delta \rho(T) \propto T$
Tetragonal structure BSCCO, $T_c \approx 90 \text{ K}$ [8–11]; TBCCO, $T_c \approx 110 \text{ K}$ [12]; TBCO, $T_c \approx 80 \text{ K}$ [13–15]	$\Delta R(T) \propto T, T \lesssim T_c/2$ $\Delta X(T) = \omega \mu_0 \Delta \lambda(T) \propto T, T \lesssim T_c/3$		Rapid growth of $R(T)$ and $X(T)$	
				$X(T) > R(T)$

$\lambda_{ab}(T)$ and $R_{ab}(T)$ curves of some YBCO single crystals possess irregularities in the intermediate temperature range.

To illustrate the data of Table 2, we show in Figs 4 and 13 experimental $R_{ab}(T)$ and $X_{ab}(T)$ curves in the ab -planes of optimally doped YBCO and BSCCO single crystals. In Fig. 13, $R_{ab}(T) = X_{ab}(T)$ for $T \geq T_c$, which corresponds to the normal skin-effect condition. Given $R_{ab}(T_c) = \sqrt{\omega \mu_0 \rho_{ab}(T_c)/2} \approx 0.12 \Omega$, we obtain the resistivity $\rho_{ab}(T_c) \approx 40 \mu\Omega \text{ cm}$. In the normal state, the temperature dependence of $R_{ab}(T)$ is adequately described above T_c by the expression $2R_{ab}^2(T)/\omega \mu_0 = \rho_{ab}(T) = \rho_0 + bT$, where $\rho_0 \approx 13 \mu\Omega \text{ cm}$, and $b \approx 0.3 \mu\Omega \text{ cm K}^{-1}$. The insets to Fig. 13 depict $R_{ab}(T)$ and $\lambda_{ab}(T) = X_{ab}(T)/\omega \mu_0$ for $T < 0.7 T_c$, plotted on a linear scale. The extrapolation of the low-temperature sections of these curves to $T = 0 \text{ K}$ yields the estimates $R_{ab}(0) = 0.5 \text{ m}\Omega$ and $\lambda_{ab}(0) = 2600 \text{ \AA}$ for this BSCCO crystal.

4.2 Complex conductivity

The conductivity components $\sigma'(T)$ and $\sigma''(T)$ are not measured directly by the ‘hot-finger’ technique, but can be derived from the measured values of $R(T)$ and $X(T)$:

$$\sigma' = \frac{2\omega \mu_0 R X}{(R^2 + X^2)^2}, \quad \sigma'' = \frac{\omega \mu_0 (X^2 - R^2)}{(R^2 + X^2)^2}. \quad (25)$$

It should be emphasized that for determining the conductivity components it is necessary to know the $R(T)$ and $X(T)$ values in absolute units (Ohms). At temperatures not very close to T_c , $R(T) \ll X(T)$ in HTSCs (see Figs 4, 7, 8, 13) and, therefore, the $\sigma''(T)$ curves are determined by the function $X(T) = \omega \mu_0 \lambda(T)$ alone and reflect the main features of the temperature behavior of the penetration depth, namely, its linear temperature dependence at low temperatures for all high-quality HTSC crystals, and the features observed for YBCO in the intermediate temperature range. The shape of the $\sigma'(T)$ curves depends on the value of the residual surface resistance $R_{\text{res}} = R(T \rightarrow 0)$ which is obtained by the extrapolation of the $R(T)$ curve to zero temperature in the region $T < T_c/3$.

It follows from relationships (25) that the $\sigma'(T)$ curve has a peak for $T < T_c$ if the value of R_{res} is sufficiently small [3, 73]:

$$R_{\text{res}} < \frac{X(0)}{3} \left. \frac{dR(T)}{dX(T)} \right|_{T \rightarrow 0}. \quad (26)$$

As R_{res} increases, the peak in $\sigma'(T)$ shifts to lower temperatures and disappears when R_{res} reaches the value equal to the right-hand side of Eqn (26). If the R_{res} value for the crystal is such that inequality (26) breaks, the conductivity $\sigma'(T)$ will monotonically increase with decreasing temperature in the range $T < T_c$. Figure 6 demonstrates both possible shapes of the $\sigma'(T)$ curves for $\text{YBa}_2\text{Cu}_3\text{O}_{6.93}$ crystal at a frequency of 9.4 GHz, namely, manifestation of the peak in the real part of the cuprate plane conductivity $\sigma'_{ab}(T)$ in the lower inset ($R_{\text{res}}^{ab} \approx 40 \mu\Omega$), and its total absence in the conductivity $\sigma'_c(T)$ along the c -axis in the upper inset ($R_{\text{res}}^{ab} \approx 800 \mu\Omega$). The higher the crystal quality, the more pronounced the conductivity $\sigma'(T)$ peak for $T < T_c$.

Figure 14 demonstrates $\sigma'_{ab}(T)$ curves extracted from the measured values of $R_{ab}(T)$ and $X_{ab}(T)$ (Fig. 8a) using formula (25) for five states of $\text{YBa}_2\text{Cu}_3\text{O}_{7-x}$ crystal with varying oxygen content.

At temperatures close to T_c , the dependence $\sigma'(T)$ in HTSCs is usually shaped like a narrow peak (see Fig. 14). Its width virtually coincides with the width of the superconducting transition in the $R(T)$ curve.

4.3 Modified two-fluid model (MTFM)

There exists a simple description of all the observed peculiarities of $Z_{ab}(T)$ and $\sigma_{ab}(T)$ dependences, which was suggested in Refs [37, 38] and later developed in Refs [73, 74]. The idea consists in the generalization of the two-fluid model by Gorter and Casimir (GC) [75] to the case of HTSC materials, whose common feature is the high T_c values. In metals, processes of inelastic scattering of quasiparticles are essential at such high temperatures and, hence, the natural modification of the GC model should incorporate the temperature dependence of the ‘normal-fluid’ quasiparticle relaxation time $\tau_{ab}(T)$. Assuming that the scattering processes in this liquid are similar to those occurring in normal metals, we utilized the Bloch – Grüneisen formula (electron – phonon scattering) for the function $\tau_{ab}(T)$ in the normal and superconducting states of HTSCs and retained the temperature-independent impurity relaxation time $\tau_{ab}(0)$ which appears in the GC model:

$$\frac{1}{\tau_{ab}(t)} = \frac{1}{\tau_{ab}(0)} \left(1 + \frac{t^5 \mathcal{J}_5(\kappa/t)/\mathcal{J}_5(\kappa)}{\beta} \right), \quad \mathcal{J}_5(\kappa/t) = \int_0^{\kappa/t} \frac{z^5 \exp(z)}{(\exp(z) - 1)^2} dz, \quad (27)$$

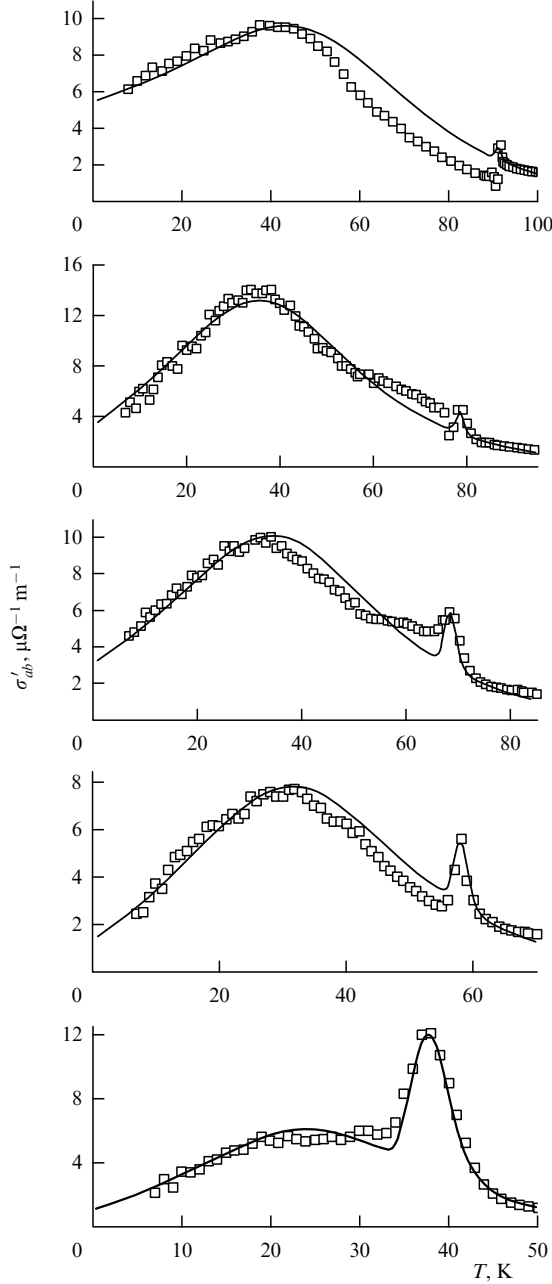


Figure 14. The real parts of conductivity $\sigma'_{ab}(T)$ (symbols) of the five states of $\text{YBa}_2\text{Cu}_3\text{O}_{7-x}$ crystal and the calculated results (solid lines) based on the modified two-fluid model (see Section 4.3) which takes into account the inhomogeneous broadening δT_c of the superconducting transition and residual surface resistance R_{res} (see Table 1).

where $t \equiv T/T_c$, $\kappa = \Theta/T_c$ (Θ is the Debye temperature), and β is the numerical parameter equal to $\tau_{ab}(T_c)/[\tau_{ab}(0) - \tau_{ab}(T_c)]$. Following the formal analogy with metals, one can say that β characterizes the ‘HTSC purity’: $\beta \approx \tau_{ab}(T_c)/\tau_{ab}(0) \ll 1$ if $\tau_{ab}(0) \gg \tau_{ab}(T_c)$. The temperature Θ in HTSCs can be estimated at several hundreds of degrees. For $T < \Theta/10$ ($\kappa > 10t$), the second summand in the parentheses in Eqn (27) is proportional to T^5 ; in the region $T > \Theta/5$ ($\kappa < 5t$), it is proportional to T . Thus, the reciprocal relaxation time (coefficient of quasiparticle decay) for $\beta < 1$ is equal to $1/\tau_{ab}(0)$ in the range $T \ll T_c$, and at higher temperatures it increases gradually following power law from $\propto T^5$ to $\propto T$ in the neighborhood of T_c , thereby

providing the linear dependence $\Delta\rho_{ab}(T) \propto 1/\tau_{ab}(T) \propto T$ for $T > T_c$.

Even though the form chosen for the function $\tau_{ab}(T)$ in Eqn (27) is over-simplified for the case of HTSC materials with complex band structure, it turned out that all common and specific features of $R_{ab}(T)$ and $\sigma'_{ab}(T)$ curves for both ranges $T < T_c$ and $T > T_c$ are adequately described by the MTFM with the single free fitting parameter κ in Eqn (27) (see Refs [3, 73] for the details). Indeed, in the case $(\omega\tau_{ab})^2 \ll 1$, which is typical for HTSC crystals at all temperatures in the frequency band around 10 GHz or below, the components of the complex conductivity $\sigma_{ab} = \sigma'_{ab} - i\sigma''_{ab}$ can be written down in a very simple form

$$\sigma'_{ab} = \frac{n_n e^2 \tau_{ab}}{m}, \quad \sigma''_{ab} = \frac{n_s e^2}{m\omega}, \quad (28)$$

where $n_{n,s}(T)$ are the densities of the normal and superconducting carriers, respectively (both have the same charge e and mass m). As $T \leq T_c$, the total carrier concentration $n = n_n + n_s$ is equal to the concentration of charge carriers in the normal state. From the measured values of $R_{ab}(T_c)$ and $X_{ab}(0)$, and the slopes dR_{ab}/dT and dX_{ab}/dT for $T \ll T_c$, one can easily derive the parameters [73]

$$\omega\tau_{ab}(T_c) = \frac{X_{ab}^2(0)}{2R_{ab}^2(T_c)}, \quad \omega\tau_{ab}(0) = \frac{dR_{ab}}{dX_{ab}} \Big|_{T \rightarrow 0} \quad (29)$$

and determine the β values from Eqn (27), which are listed in Table 1. Now, making use of the measured dependence $n_s(T)/n = \sigma''_{ab}(T)/\sigma''_{ab}(0) = \lambda_{ab}^2(0)/\lambda_{ab}^2(T)$ and, hence, determining the function $n_n(T)/n = 1 - n_s(T)/n$, one can choose the parameter κ for the sample of interest, using Eqns (27), (28), to describe, first, by the general formula

$$R_{ab} = \text{Re} \left(\sqrt{\frac{i\omega\mu_0}{\sigma' - i\sigma''}} \right), \quad (30)$$

the experimental $R_{ab}(T)$ curves and, next, by Eqn (25), the real part $\sigma'_{ab}(T)$ of the conductivity. The solid lines in Fig. 14 are plotted for the comparison of the experimental data with the calculated results produced by the above procedure. In addition, we took account of the inhomogeneous broadening δT_c of the superconducting transition (see Table 1) following the approach [3, 73] that describes the peak in the conductivity $\sigma'(T)$ at a temperature of $T_m = T_c - \delta T_c$, which is close to the critical one. The relative amplitude $[\sigma'(T_m) - \sigma(T_c)]/\sigma(T_c)$ of this peak is inversely proportional to the frequency and becomes smaller, the narrower the superconducting transition (the smaller δT_c). Furthermore, when making comparisons with the experimentally found surface resistance, we added to the $R(T)$ value calculated using formula (30) the temperature-independent R_{res} value taken from the same experiment (see Table 1). That is why the $\sigma'_{ab}(T)$ curves in Fig. 14 then calculated by formula (25) do not tend to zero as $T \rightarrow 0$, although the MTFM assumes that the density $n_n = 0$ at $T = 0$ and, according to Eqn (28), the conductivity $\sigma_{ab}(0) = 0$. The contribution R_{res} to the function $R(T)$ being calculated is essential for most HTSC crystals in which $R_{\text{res}}/R(T_c) > 10^{-3}$. The solid lines in Fig. 13 depict the $X_{ab}(T)$ and $R_{ab}(T)$ dependences calculated in the framework of the MTFM with the parameters $\omega\tau_{ab}(T_c) = 0.9 \times 10^{-2}$, $\beta = 2$, and $\kappa = 3$ and the measured $\sigma''_{ab}(T)$ values. In this case, we have added to $R_{ab}(T)$ defined by Eqn (30) the constant

$R_{\text{res}} = 0.5 \text{ m}\Omega$. It is seen that the agreement between the calculated and experimental curves is fairly good throughout the temperature interval $5 \leq T \leq 160 \text{ K}$.

4.4 On the residual surface resistance

Whereas the R_{res} value in classical superconductors is clearly defined as a level of the plateau in the $R(T)$ curve for $T < T_c/4$, no such plateau appears in HTSC crystals, so that by R_{res} is meant the $R(T = 0)$ value obtained by extrapolating the linear section of the $R(T)$ curve for $T \ll T_c$ to zero temperature. It was experimentally established for classical superconductors that the quantity $R_{\text{res}} \propto \omega^2$ and is determined by various defects in the surface layer of the sample [62, 76]; based on this fact, it is usually agreed that the smaller R_{res} , the higher the sample quality. In HTSC materials, the residual resistance also varies quadratically with frequency, but it exceeds the R_{res} value in conventional superconductors by a factor of several dozens even in the best crystals. When it is considered that the R_{res} value has not been noticeably reduced over the last 10 years of developing the methods of growing HTSC crystals and that the temperature behavior of conductivity $\sigma'(T)$ in samples of identical chemical composition alters radically with changing R_{res} , then it becomes clear that elucidation of the nature of residual losses in HTSC materials is a highly topical problem.

In some works (see, for example, Ref. [77]), the origin of the residual losses in HTSCs was attributed to the presence of a fraction n_0 of carriers that remained unpaired at $T = 0$. The R_{res} value was estimated by the formula $R = \omega^2 \mu_0^2 \sigma' \lambda^3 / 2$, following from Eqn (30) for $T < T_c$, with the nonzero conductivity $\sigma'(0) = n_0 e^2 \tau(0) / m$ given by Eqn (28). However, it can easily be shown that the R_{res} values thus determined must satisfy inequality (26). Otherwise, as may be the case for HTSC crystals [3, 73], the n_0 value would exceed the total carrier concentration n . Developing the traditional approach, the authors of many papers assigned the residual resistance to various surface imperfections and the losses were accounted for by the presence of weak links [78–80], twin boundaries [80, 81], normally conducting clusters [82], etc. Estimates show, however, that the contribution from such losses is small compared to the R_{res} values measured in the HTSC materials. In addition, the residual surface resistance is approximately the same in the cuprate planes of perfect copper oxide HTSC crystals with various chemical compositions, prepared by different methods, containing twins or not, and with a freshly cleaved surface or as-grown surface: $R_{\text{res}} \sim 100 \text{ }\mu\Omega$ at a frequency of 10 GHz. This fact indicates that the origin of residual losses has an ‘intrinsic’ character and is inherent in all high-quality HTSC crystals. It is most likely associated with the structural peculiarities of these materials, namely, with the pronounced layered structure of these compounds [61]. In other words, the current in the surface layer of HTSC crystals may flow in a nonsuperconducting portion of the layer possessing a finite resistivity ρ_n . In the phenomenological model under discussion, this additional contribution can be taken into account as a circuit element ρ_n connected in parallel to the two-fluid circuit characterized by Eqn (28), i.e., as a resistivity $\rho = 1/\sigma'$ shunted by a kinetic inductance $l = 1/\omega\sigma''$ (the parallel connection of ρ and l corresponds to the coupling between current and field adopted in the two-fluid model). Evidently, the complex circuit impedance will consist of the imaginary part $iX = i\omega\mu_0\lambda$ for $T < T_c$ and the sum of two real terms: the ordinary $R = \omega^2 \mu_0^2 \lambda^3 / 2\rho$, and $R_0 = \omega^2 \mu_0^2 \lambda^3 / 2\rho_n$. At $T = 0$,

when $R(0) = 0$, the latter can play the role of a residual surface resistance R_{res} proportional to ω^2 , as follows from experiments. At a frequency of 10 GHz and for the $R_{\text{res}} \approx 100 \text{ }\mu\Omega$ and $\lambda(0) \approx 0.2 \text{ }\mu\text{m}$ values characteristic of HTSC crystals, one obtains a typical metallic value of $\rho_n(0) \approx 25 \text{ }\mu\Omega \text{ cm}$. According to our procedure of comparison with the experimental $R(T)$ curves, one must also require that R_0 be independent of the temperature $T \ll T_c$. This is possible if $\rho_n(T) \propto \lambda^3(T)$, i.e., $\rho_n(T)$ should vary linearly with temperature as $T \ll T_c$: $\rho_n(t) = \rho_n(0)(1 + 1.5\alpha t)$, where α is the slope of the $\sigma''(t)$ curve for $t \ll 1$ in a given sample:

$$\frac{\sigma''(t)}{\sigma''(0)} = \frac{n_s(t)}{n} = \frac{\lambda^2(0)}{\lambda^2(t)} \approx (1 - \alpha t). \quad (31)$$

One can easily verify that the coefficients $\rho_n(0)$ and $1.5\alpha\rho_n(0)/T_c$ for BSCCO single crystal (see Fig. 13) are approximately equal to $\rho_{ab}(0)$ and b in the resistivity $\rho_{ab}(T) = \rho_{ab}(0) + bT$ of this sample in the normal state, i.e., $\rho_n(T) \approx 2R^2(T)/\omega\mu_0$, where $R(T)$ is the portion of the $R_{ab}(T)$ line for $T > T_c$ in Fig. 13, extrapolated to the superconducting region $T < T_c$, down to $T = 0$.

It would be natural to complete the presentation of the MTFM by writing down formulae describing the experimental data for $n_s(T)/n = \sigma''_{ab}(T)/\sigma''_{ab}(0)$. Several versions of such empirical formulae were given elsewhere [3, 37, 38, 73, 74]. Notice only that all of them take the form of Eqn (31) as $T \ll T_c$ because all $\sigma''_{ab}(T)$ curves for HTSC single crystals are characterized by linear dependence at low temperatures.

4.5 Inference concerning the impedance $Z_{ab}(T)$ and conductivity $\sigma_{ab}(T)$

Thus, one can describe the characteristic features of $Z_{ab}(T)$ and $\sigma_{ab}(T)$ curves in the ab -planes of optimally doped HTSCs by generalizing the GC two-fluid model. For this purpose we introduced the temperature dependence of quasiparticle relaxation time according to the Bloch–Grüneisen law and replaced the well-known temperature dependence of the density of superconducting carriers in the GC model, $n_s = n(1 - t^4)$, by one of the functions deduced in Ref. [3], which changes linearly with the temperature for $t \ll 1$ [see Eqn (31)]. As a result, it follows from the MTFM formulae (27)–(31) that at low temperatures ($t \ll 1$) and low frequencies ($\omega\tau_{ab}(0) < 1$), all the $Z_{ab}(T)$ and $\sigma_{ab}(T)$ curves have a linear section: $\sigma'_{ab} \propto \alpha t/\beta$, since $n_n/n \approx \alpha t$ and $\tau_{ab} \approx \tau_{ab}(0) \approx \tau_{ab}(T_c)/\beta$; $\Delta\sigma''_{ab} \propto -\alpha t$ from Eqn (31); $R_{ab} \propto \alpha t/\beta$ in accordance with Eqn (30), and $\Delta X_{ab} \propto \Delta\lambda_{ab} \propto \alpha t/2$. As the temperature increases, the $\sigma'_{ab}(t)$ function passes through a maximum for $t < 0.5$ if the residual surface resistance R_{res} is so small that inequality (26) is fulfilled. This peak arises from the superposition of two competing effects: a decrease in the number of normal carriers with decreasing temperature for $t < 1$, and an increase in the relaxation time, which saturates at $t \sim \beta^{1/5}$, where the impurity scattering starts to dominate. If inequality (26) is not fulfilled, $\sigma'_{ab}(T)$ monotonically decreases with temperature elevation. There is no BCS coherence peak [1] in the conductivity $\sigma'_{ab}(t)$ in the range nearby $T \sim 0.85 T_c$. Usually, the $\sigma'_{ab}(T)$ curve in HTSC crystals has a narrow peak near T_c (see Fig. 14), whose width virtually coincides with the width of the transition from the normal to superconducting state in the $R_{ab}(T)$ curve. The origin of this peak can be explained in terms of an effective medium model, where the inhomogeneous broadening of the superconducting transition is taken into account.

It also follows from the MTFM that the missing of the broad peak from $R_{ab}(t)$ at $t \sim 0.5$ in $\text{YBa}_2\text{Cu}_3\text{O}_{7-x}$ with oxygen deficiency and in high-quality tetragonal HTSC single crystals is due to a less rapid increase in $\tau_{ab}(T)$ with decreasing temperature. In other words, the value of β is the smallest for the case of optimally doped YBCO crystals (see Table 1).

It is natural to compare the tenets of the MTFM with the results of microscopic theories. First of all, there is nothing foreign in introducing the function $1/\tau_{ab}(T) \propto T^5$ in Eqn (27) for the purpose of characterizing scattering in the superconducting state of HTSCs. A similar temperature dependence of the quasiparticle relaxation rate follows from the strong coupling model if the phonon corrections to the electromagnetic vertex are taken into account [83]. Using this result, the authors of Ref. [84] proved that the peaks in the temperature dependences of $R_{ab}(T)$ and $\sigma'_{ab}(T)$, which are characteristic features of YBCO, can be obtained even on the basis of the conventional isotropic model [83], although quantitative agreement between this model and experimental findings is out of the question. As was shown in Refs [3, 41], the simple formula (31) defining the linear low-temperature dependence of the magnetic field penetration depth in the ab -plane of HTSC crystals is consistent with a spin fluctuation d-wave model [85] in a unitary scattering limit [86]. Notice that the presence of quasi-one-dimensional sections of the electronic spectrum in HTSCs and their related square-root van-Hove singularities in the density of states lead, according to Ref. [87], to the d-wave pairing caused by anisotropic electron–phonon coupling. Other origins of d -symmetry of the order parameter were considered in Refs [88, 89] within the phonon mechanism.

In the framework of the MTFM, the linear low- T dependence of the real part $\sigma'_{ab}(T)$ of the conductivity in Eqn (28) is consistent with a constant scattering rate. While the assumption of a Drude form of the microwave conductivity is supported by the d-wave microscopic analysis [86], it was shown that pair correlations in the usual impurity scattering model lead to a strong T -dependence of the scattering time (neglecting vertex corrections), namely, $\tau_{ab}(T) \propto T$ in the unitary limit or $\tau_{ab}(T) \propto 1/T$ in the Born limit. The authors of Refs [90, 91] argued that the experimental finding of $\sigma'_{ab}(T) \propto T$ for $T \ll T_c$ can be explained if the quasiparticle density varies proportionally to T (as indeed happens in the d-wave pairing) and if the effective quasiparticle scattering time $\tau_{ab}(T)$ saturates at low T . Various possible physical mechanisms of the temperature and energy dependences of τ_{ab} , which may provide the required saturation of $\tau_{ab}(T)$ at low T , were discussed in Refs [90, 91]. As was argued in Ref. [92], the vertex corrections can also modify the low-temperature conductivity.

Nevertheless, the microscopic models aimed at describing the microwave response using a pure d-wave order parameter symmetry cannot account for the linear portion of the $R_{ab}(T)$ curves extending to $T_c/2$ (at frequencies of 10 GHz and below) in tetragonal HTSC crystals, for the observation of different slopes of the $\sigma''_{ab}(T)$ curves for $T \ll T_c$ in YBCO crystals, and for the features of $\sigma''_{ab}(T)$ in the intermediate temperature range (see Table 2). These observations have caught the attention of a number of theoreticians [93–99] and were tentatively attributed to the manifestation of a mixed (d + s)-wave symmetry of the order parameter. Most studies deal with the low-temperature variations of the London penetration depth. In

particular, the (d + s) model was generalized in Ref. [96] by taking the normal state anisotropy into account. This is the realistic approach to HTSCs with an orthorhombic distortion. Additionally, taking into consideration the impurity scattering in the model [96], we have calculated in Ref. [99] the temperature dependences of the penetration depth $\lambda_{ab}(T)$, which demonstrated the different slopes of $\Delta\lambda_{ab}(T) \propto T$ curves for $T < T_c/4$ in various $\text{YBa}_2\text{Cu}_3\text{O}_{6.93}$ samples, and also the features of $\Delta\lambda_{ab}(T)$ in the intermediate temperature range nearby $T \sim T_c/2$. A quantitative comparison of the latter calculation with the experimental data has been performed in the CSC thesis [15].

5. Pseudogap effect

In past years, much effort was devoted to studying the nature and properties of pseudogap states of the HTSC phase diagram corresponding to a lower concentration p of holes per copper atom in comparison with the optimal value $p \approx 0.16$. Currently, the origin of the pseudogap remains unclear. Proposed theoretical scenarios can be divided into two categories. One is based on the idea that the pseudogap is due to precursor of superconductivity, where pairing takes place at a certain pseudogap transition temperature $T^* > T_c$ but achieves coherence only at $T = T_c$. The other assumes that the pseudogap state is not related to superconductivity per se, but rather competes with it, and is caused by dynamical fluctuations of some kind, such as spin, charge, or structural, or by charge density waves with d-symmetry of the order parameter (d-density wave — DDW). These scenarios treat anomalies of electronic properties in underdoped HTSCs, observed at temperatures both above T_c and in its vicinity [100–103].

When approaching the dielectric phase ($p \approx 0.05$), a competition among pseudogap and superconducting order parameters develops most effectively and for $T \ll T_c$ results in peculiarities of the superfluid density $n_s(T, p)$ as a function of T and p .

In a clean BCS d-wave superconductor (DSC), the dependence $\Delta n_s(T) \equiv n_s(T) - n_0$ is linear with temperature for $T \ll T_c$: $\Delta n_s(T) \propto (-T/\Delta_0)$, where $n_0 \equiv n_s(0)$ and $\Delta_0 \equiv \Delta(0)$ are the superfluid density and the superconducting gap amplitude at $T = 0$, respectively. This dependence is reliably confirmed by the measurements of the ab -plane London penetration depth $\lambda_{ab}(T) = \sqrt{m^*/\mu_0 e^2 n_s(T)}$ in optimally doped ($p = 0.16$) HTSC single crystals: $\Delta\lambda_{ab}(T) \propto T$ for $T < T_c/3$ (see Table 2). The derivative $|dn_s(T)/dT|$ as $T \rightarrow 0$ determines the n_0/Δ_0 ratio. If thermally excited fermionic quasiparticles are the only important excitations even for $p < 0.16$, the slope of $n_s(T)$ curves for $T \ll T_c$ remains proportional to the $n_0(p)/\Delta_0(p)$ ratio: $|dn_s(T)/dT|_{T \rightarrow 0} \propto n_0(p)/\Delta_0(p)$. The measurements of $\lambda_{ab}(0)$ in underdoped HTSCs showed that the superfluid density $n_0(p) \propto \lambda_{ab}^{-2}(0)$ increases approximately linearly with $p > 0.08$, reaching its maximum value at $p \approx 0.16$ [104, 105].

When p is lowered below 0.16, the role of electron correlations and phase fluctuations in HTSCs rises. The generalized Fermi-liquid models (GFLs) allow for this effect through p -dependent Landau parameter $L(p)$ [106–108] including $n_0(p)$. The values of $\Delta_0(p)$ and $L(p)$ determine the p -dependence of the derivative $|dn_s(T)/dT|_{T \rightarrow 0} = L(p)/\Delta_0(p)$. In the model [106], the ratio $L(p)/\Delta_0(p)$ does not depend on p , while the model [107] predicts

$L(p)/\Delta_0(p) \propto p^{-2}$. The measurements on $\text{YBa}_2\text{Cu}_3\text{O}_{7-x}$ single crystals [109] and oriented powders [110] with the hole concentration $p \gtrsim 0.1$ showed that the slopes of $n_s(T)$ dependences as $T \rightarrow 0$ are either slightly p -dependent [109], which agrees with the inference of Ref. [106], or diminish with decreasing $p \leq 0.16$ [110], which contradicts the predictions of GFL models [106–108].

Along with the above concept, there are a number of pseudogap concepts [100–103] proposed in order to describe the collapse of single-particle density of excited states near the Fermi level, experimentally demonstrated in underdoped HTSCs for $T \gtrsim T_c$ by various techniques. In Ref. [111], the pseudogap order parameter was found to have the same d -wave symmetry as the superconducting one; it influences the quasiparticle spectrum when $T < T_c$, as well. In the model [112], based on the formation of pair electron excitations with finite momentum for $T^* > T_c$, this influence leads to a rise in $\Delta_0(p)$ and a decrease in $n_0(p)$ with a lowering of p . Hence, a decrease in the derivative $|dn_s(T)/dT|_{T \rightarrow 0} \propto n_0(p)/\Delta_0(p)$ might be expected. The $n_s(T, p)/n_0$ curves numerically calculated in Ref. [113] show that their slopes decrease as $T \ll T_c$ with a decrease in concentration p .

An opposed behavior of $|dn_s(T)/dT|$ follows from the DDW scenario of pseudogap [114]. In this model, a DDW order parameter $W(p, T)$ is directly introduced into the quasiparticle band structure. At low energies, the excitation spectrum of the DDW consists of conventional fermionic particles like that of DSC with which it competes for $p < 0.2$. The DSC gap $\Delta_0(p)$ steadily vanishes with decreasing p , whereas the sum of zero-temperature squares $\Delta_0^2(p) + W_0^2(p)$ remains constant [115]. As a result, the DDW model predicts a growth in the slope of the $n_s(T, p)/n_0$ curves at low T and $p < 0.1$.

At the same time, the modern concept [116] is that the DDW pseudogap weakly influences the field penetration depth $\lambda_c(T, p)$ for the currents directed perpendicular to CuO_2 planes. A rapid decline in the interlayer coupling integral $t_\perp(p)$ as the concentration p decreases must have a decisive impact on $\lambda_c(T, p)$.

Sections 5.1 and 5.2 aim at experimental verification of the above-mentioned theoretical speculations.

5.1 Superfluid density $n_s(T, p)$

In Fig. 12, the linear zero-temperature extrapolation (dashed lines) of the $\lambda_{ab}(T)$ dependences for $T < T_c/3$ gives the following $\lambda_{ab}(0)$ values: 152, 170, 178, 190, and 198 nm for $p = 0.16, 0.12, 0.106, 0.092$, and 0.078 , respectively (see Table 1). As follows from Fig. 15, halving the hole concentration (from $p = 0.16$ to $p = 0.078$) results in an approximately two times smaller $\lambda_{ab}^{-2}(0) = n_0\mu_0e^2/m^*$ value [117]. Similar behavior of $n_0(p) \propto p$ within the range $0.08 < p \leq 0.16$ was observed earlier by other groups [104, 105]. It is easily seen that this dependence contradicts Uemura's relation $n_0(p) \propto T_c(p)$ [118].

To the best of our knowledge, there are no measurement data on the $n_0(p)$ in HTSCs for $p < 0.08$. As for theoretical predictions, the linear dependence $n_0(p) \propto p$ extends down to $p = 0$ in the model [106]. In the DDW model [114, 115, 119], $n_0(p) \propto p$ in the range $0.07 < p < 0.17$, where the DSC order parameter grows from zero to its maximal value according to the phase diagram in Fig. 16; however, $n_0(p)$ remains nonzero as $\Delta_0(p) \rightarrow 0$ (see Fig. 1 from Ref. [119]). The latter inference agrees with the data in Fig. 15.

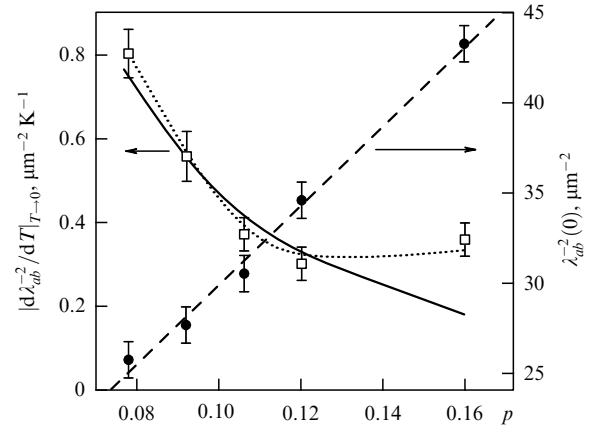


Figure 15. The values of $\lambda_{ab}^{-2}(0) = n_0\mu_0e^2/m^*$ (right scale) and slopes $|d\lambda_{ab}^{-2}(T)/dT|_{T \rightarrow 0} = \mu_0e^2/m^*|dn_s(T)/dT|_{T \rightarrow 0}$ (left scale) as the functions of doping $p = 0.16 - \sqrt{(1 - T_c/T_{c,\max})}/82.6$ with $T_{c,\max} = 92$ K in $\text{YBa}_2\text{Cu}_3\text{O}_{7-x}$. Error bars correspond to measurement accuracy. The dashed and dotted lines guide the eye. The solid line represents the $|dn_s(T)/dT| \propto p^{-2}$ dependence.

In Fig. 15, we also plotted the p -dependences of the slopes $|d\lambda_{ab}^{-2}(T)/dT|_{T \rightarrow 0} \propto |dn_s(T)/dT|_{T \rightarrow 0}$ of the $\lambda_{ab}^{-2}(T)$ curves obtained from $\lambda_{ab}(T)$ data for $T < T_c/3$ in Fig. 12. The value of $|d\lambda_{ab}^{-2}(T)/dT|$ changes slightly in the range $0.1 < p \leq 0.16$, in accordance with model [106] and measurements on $\text{YBa}_2\text{Cu}_3\text{O}_{7-x}$ [109, 110] with hole concentrations $p \gtrsim 0.1$. However, it grows dramatically for $p \lesssim 0.1$, namely, the slope of $\lambda_{ab}^{-2}(T)$ increases by a factor of 2.5 with p decreasing from 0.12 to 0.08. The $|d\lambda_{ab}^{-2}(T)/dT| \propto p^{-2}$ dependence is shown by a solid line in Fig. 15 and fits the data [107] when $p \leq 0.12$. The dotted line drawn through all the $|d\lambda_{ab}^{-2}(T)/dT|$ experimental points in Fig. 15 qualitatively agrees with the behavior of this quantity in the DDW model [115, 119].

One more confirmation of this scenario of pseudogap effect is the temperature variation of the superfluid density $\Delta n_s(T)$ at low T in the heavily underdoped $\text{YBa}_2\text{Cu}_3\text{O}_{7-x}$. Normalized $\lambda_{ab}^2(0)/\lambda_{ab}^2(T) = n_s(T)/n_0$ dependences obtained

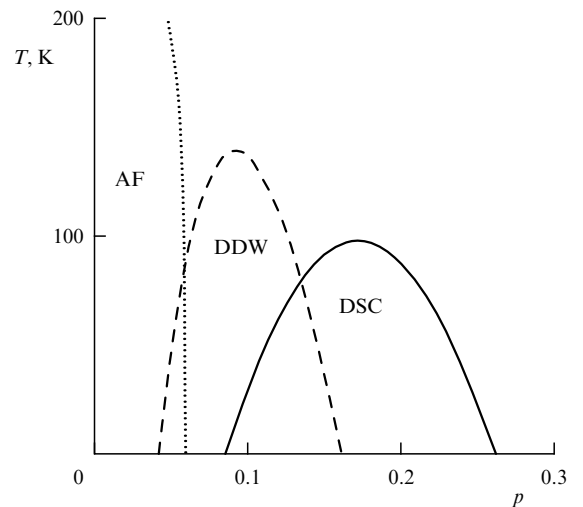


Figure 16. Schematic T - p phase diagram based on calculations of Ref. [120] for a DDW-pseudogap modelled HTSC. AF is the three-dimensional antiferromagnetic phase. The system is an insulator in the AF state, a metal in the DDW and DDW + AF states, and a superconductor in the DSC and DDW + DSC states.

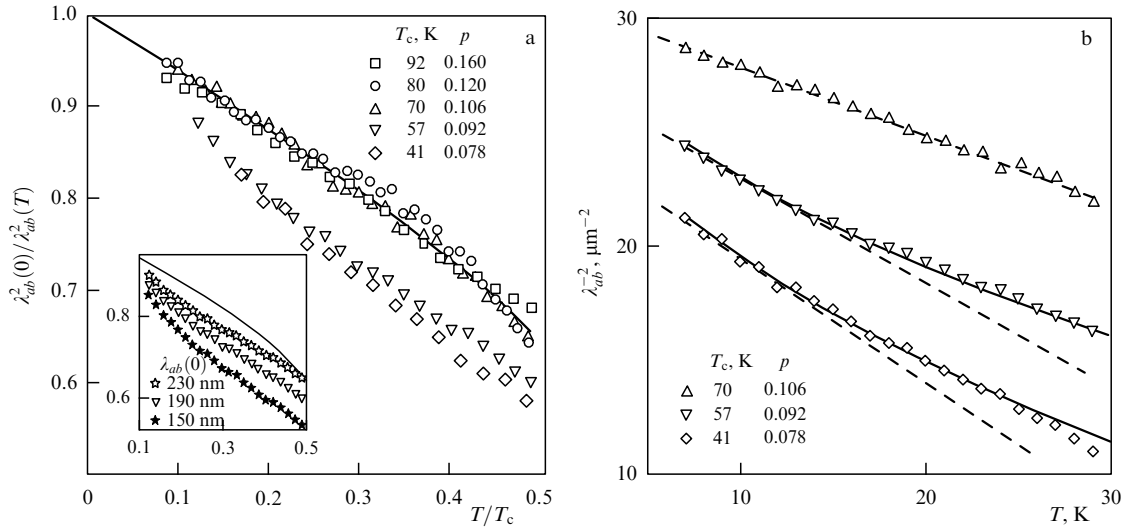


Figure 17. (a) $\lambda_{ab}^2(0)/\lambda_{ab}^2(T) = n_s(T)/n_0$ dependences for $T < T_c/2$ in $\text{YBa}_2\text{Cu}_3\text{O}_{7-x}$ with different dopings. The solid line is the $\lambda_{ab}^2(0)/\lambda_{ab}^2(T)$ dependence in a clean BCS d-wave superconductor (DSC). The inset shows the experimental $n_s(T)/n_0$ curve for $p = 0.092$ (triangles) and those obtained using $\lambda_{ab}(0)$ increased (open stars) and decreased (closed stars) by 40 nm. (b) Comparison of experimental $\lambda_{ab}^{-2}(T) \propto n_s(T)$ curves (symbols) with linear $\Delta\lambda_{ab}^{-2}(T) \propto (-T)$ (dashed straight lines) and root $\Delta\lambda_{ab}^{-2}(T) \propto (-\sqrt{T})$ (solid lines) dependences for moderately doped ($p = 0.106$, $x = 0.33$) and heavily underdoped ($p = 0.092$, $x = 0.40$; $p = 0.078$, $x = 0.47$) $\text{YBa}_2\text{Cu}_3\text{O}_{7-x}$ crystals.

from the data in Fig. 12 for $T < T_c/2$ are shown in Fig. 17a for all states of $\text{YBa}_2\text{Cu}_3\text{O}_{7-x}$ crystal with different p values (symbols). The solid line represents the $n_s(T)/n_0$ dependence in DSC. The evident peculiarity of the heavily underdoped states ($p = 0.078$ and $p = 0.092$) is the concavity of $n_s(T)/n_0$ curves and their deviation from the DSC dependence and the curves for $p = 0.16$, 0.12 , and 0.106 . It should be noted that this peculiarity does not strongly depend on the $\lambda_{ab}(0)$ values. This is demonstrated in the inset to Fig. 17a, where experimental $n_s(T)/n_0$ data at $p = 0.092$ (triangles) are compared to the ones obtained using $\lambda_{ab}(0)$ increased (open stars) and decreased (closed stars) by 40 nm. Actually, the latter value is much higher than the experimental uncertainty (~ 5 nm) of determining $\lambda_{ab}(0)$.

The behavior of $n_s(T)/n_0$ in Fig. 17a contradicts the conclusions of the pseudogap conception [113] as a precursor to superconductivity, but agrees with the DDW scenario [115]. According to Ref. [115], at temperatures much smaller than the relevant energy scales W_0 and Δ_0 , only the nodal regions close to the points $(\pi/2, \pi/2)$ and symmetry-related points on the Fermi surface will contribute to the suppression of the superfluid density. An expansion of these regions leads to the linear temperature dependence of $n_s(T)$ for the optimally and moderately doped HTSC samples in a fairly wide range of low temperatures. Under such concentrations p , for which Δ_0 is larger than or comparable to W_0 (see Fig. 16), the parameter W_0 plays a subleading role with relation to Δ_0 in determining the temperature dependence of the superfluid density. However, the situation is quite different for the heavily underdoped samples. As the DDW gap is much wider than the superconducting gap in these samples, W_0 becomes dominant around the nodes. Though in the asymptotically low-temperature regime, as before, the $n_s(T)$ function varies linearly with T , there appears an intermediate temperature range over which the $n_s(T)$ actually behaves as \sqrt{T} . It is worth emphasizing that the authors of Ref. [115] stated that these peculiarities are independent of the precise $W_0(p)$ and $\Delta_0(p)$ functional forms. The only input that is needed reduces to the

existence of DDW order, which diminishes with increasing p , and complementary development of the DSC order. The DDW order ‘eats away’ part of the superfluid density from an otherwise pure DSC system. Actually, in the intermediate temperature range $0.1 T_c < T \lesssim 0.5 T_c$, the experimental data for $n_s(T)$ in $\text{YBa}_2\text{Cu}_3\text{O}_{6.60}$ and $\text{YBa}_2\text{Cu}_3\text{O}_{6.53}$ with $p < 0.1$ are not linear but exhibit \sqrt{T} -dependences. This is confirmed in Fig. 17b, where the measured $\lambda_{ab}^{-2}(T) \propto n_s(T)$ curves are compared with linear ($\propto T$) in $\text{YBa}_2\text{Cu}_3\text{O}_{6.67}$ ($p = 0.106$) and \sqrt{T} -dependences $\Delta\lambda_{ab}^{-2}(T) = -3\sqrt{T}$ (λ_{ab} and T are expressed in μm and K, respectively) in $\text{YBa}_2\text{Cu}_3\text{O}_{6.60}$ ($p = 0.092$) and $\Delta\lambda_{ab}^{-2}(T) = -3.5\sqrt{T}$ in $\text{YBa}_2\text{Cu}_3\text{O}_{6.53}$ ($p = 0.078$). The dashed straight lines in Fig. 17b correspond to the linear extrapolation of $\lambda_{ab}(T)$ curves presented in Fig. 12 for $T < T_c/3$ to the region of high temperatures.

The peculiarities of $\lambda_{ab}^{-2}(T)$ with $p < 0.1$ in Fig. 17 are accompanied by the appearance of inflections of the resistivity in the two lower $\rho_{ab}(T)$ curves in $\text{YBa}_2\text{Cu}_3\text{O}_{7-x}$ crystal at $x = 0.40$ and $x = 0.47$ in Fig. 9 around $T \sim 100$ K. The evolution of $\rho_c(T)$ dependences with doping x correlates with the temperature behavior of the imaginary part of conductivity $\sigma_c''(T, p) = \lambda_c^{-2}(T, p)/\omega\mu_0$ along the c -axis.

5.2 The c -axis penetration depth $\lambda_c(T, p)$

The solid symbols in Fig. 18a display the $\lambda_c^2(0)/\lambda_c^2(T) = \sigma_c''(T)/\sigma_c''(0)$ dependences for $T \leq T_c/2$ for three states of $\text{YBa}_2\text{Cu}_3\text{O}_{7-x}$ crystal with $T_c = 92$ K, $T_c = 70$ K, and $T_c = 41$ K [121]. Table 1 contains the values of the penetration depth $\lambda_c(0)$ at $T = 0$ and the exponents α in the measured $\lambda_c(T) - \lambda_c(0) = \Delta\lambda_c(T) \propto T^\alpha$ dependences for $T \leq T_c/3$. The $\lambda_{ab}^2(0)/\lambda_{ab}^2(T)$ (open circles in Fig. 18a) and $\lambda_c^2(0)/\lambda_c^2(T)$ curves coincide in the optimally doped ($x = 0.07$, $p = 0.16$) $\text{YBa}_2\text{Cu}_3\text{O}_{6.93}$ crystal, as should be the case in the anisotropic 3D superconductor [39]. With the decrease in p , the slopes of $\lambda_c^2(0)/\lambda_c^2(T)$ curves for $T < T_c/3$ reduce substantially. In the model [122], such a behavior of $\sigma_c''(T, p)$ corresponds to a decrease in the interlayer coupling integral $t_\perp(p)$ between the cuprate planes (solid and dashed

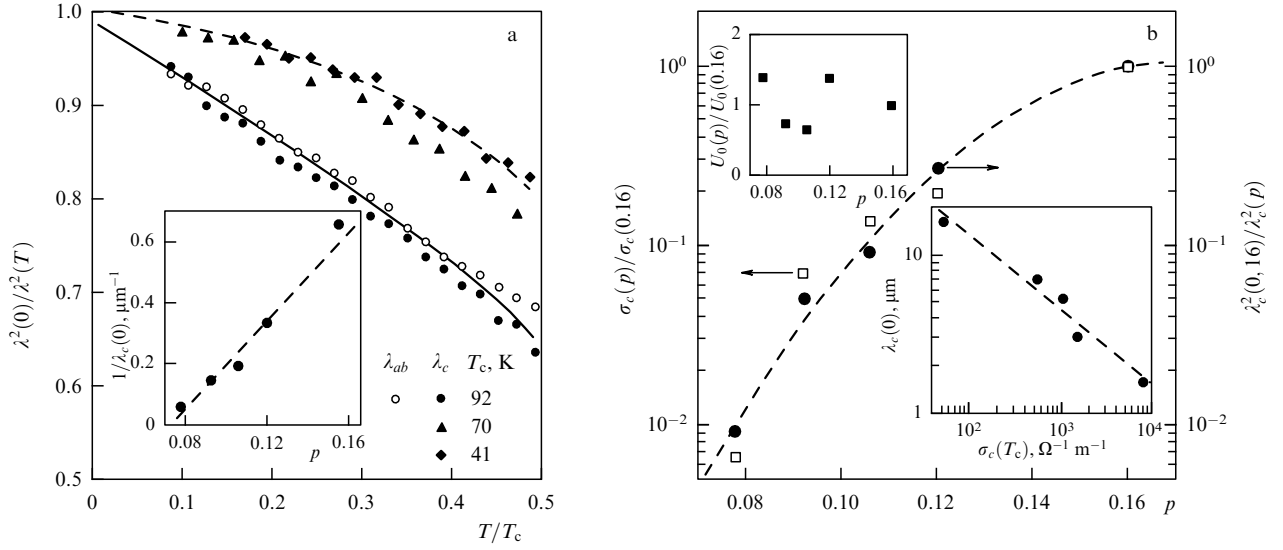


Figure 18. (a) $\lambda_{ab}^2(0)/\lambda_{ab}^2(T)$ dependence (open symbols) in YBa₂Cu₃O_{6.93} and $\lambda_c^2(0)/\lambda_c^2(T)$ (closed symbols) measured for three states of the YBa₂Cu₃O_{7-x} crystal with $T_c = 92$ K, $T_c = 70$ K and $T_c = 41$ K. Solid and dashed lines stand for the dependences $\lambda_c^2(0)/\lambda_c^2(T)$ calculated in Ref. [63] for YBa₂Cu₃O_{7-x} with different oxygen deficiencies. The inset shows $1/\lambda_c$ at $T = 0$ as a function of doping p . (b) Doping dependences of $\lambda_c^2(p)/\lambda_c^2(0.16)$ at $T = 0$ and $\sigma_c(p)/\sigma_c(0.16)$ at $T = T_c$. Their ratio $U_0(p)/U_0(0.16)$ is depicted in the upper inset. The lower inset portrays $\lambda_c(0)$ vs. $\sigma_c(T_c)$ plot.

lines in Fig. 18a represent the numerical results [122] for $p = 0.16$ and $p \sim 0.1$, respectively) and correlates with the crossover from Drude ($p = 0.16$) c -axis conductivity to the hopping one ($p < 0.16$) as $T > T_c$.

So, the low- T dependences of $\lambda_c(T)$ are well described without taking pseudogap effects into consideration. Let us consider now their possible manifestations in the doping dependence of the c -axis penetration depth.

From the inset to Fig. 18a it follows that the reciprocal value $1/\lambda_c(0, p)$ of the penetration depth at $T = 0$ depends linearly on p and, in contrast to $n_0(p)$ in Fig. 15, it vanishes at $p \approx 0.07$, which is near the value where T_c vanishes, too (see Fig. 16).

There are several theoretical models [63, 123] and experimental confirmations [124] of the direct proportionality of $\lambda_c^{-2}(0)$ to $\sigma_c(T_c)$ in HTSCs. In the simplest theory, this correlation follows from the relationship $\lambda_c^{-2} \propto J_c$, where J_c is the c -axis critical current in the d-wave superconductor with anisotropic interlayer scattering and weak interlayer coupling. The $J_c(0)$ value is determined by both the superconducting gap Δ_0 and conductivity $\sigma_c(T_c)$. The symbols in the lower inset to Fig. 18b show the data fitted by the dashed line $\log \lambda_c(0) = -0.5 \log \sigma_c(T_c) + 2.1$ (λ_c is measured in μm , and σ_c in $\Omega^{-1}\text{m}^{-1}$). The numerical constant 2.1 defines a proportionality factor $U_0(p)$ in the $\lambda_c^{-2}(0, p) = U_0(p) \sigma_c(T_c, p)$ relationship. The values of $\lambda_c^2(0.16)/\lambda_c^2(p)$ at $T = 0$ and $\sigma_c(p)/\sigma_c(0.16)$ at $T = T_c$ in the range $0.07 < p < 0.16$ are given in Fig. 18b. Their ratio $U_0(p)/U_0(0.16)$ is demonstrated in the upper inset to Fig. 18b. In the framework of the DDW model, the factor $U_0(p)$ is determined by the p -dependences of $\Delta_0(p)$, and $W_0(p)$ and chemical potential $\mu(p)$. As shown in Ref. [116], the opening of the DDW gap can lead to an increase, as well as to a decrease, in $U_0(p)$. This depends on the position of the Fermi surface with respect to the DDW gap, but in any case the coefficient $U_0(p)$ changes less than twice over the range $0.07 < p < 0.16$, which corresponds to the measurement data in Fig. 18b. Therefore, DDW pseudogap does not virtually influence the $\lambda_c(0, p)$ dependence. The behavior of $\lambda_c(0, p)$

is governed by a strong decrease in the interlayer coupling integral $t_{\perp}(p) \propto \sigma_c(T_c, p)$ with a decrease in p in YBa₂Cu₃O_{7-x} [125], leading to a two orders of magnitude change in the $\sigma_c(p)/\sigma_c(0.16)$ value at $T = T_c$ in Fig. 18b.

6. Conclusions

First of all, I would like to formulate the results of microwave investigations into HTSC crystals.

High-precision measurements of the temperature dependences of the surface impedance in the ab -planes of optimally doped HTSCs allow one to conclude that if strong electron–phonon coupling and anisotropy of the order parameter are taken into account, the Fermi-liquid approach is adequate to describe the main experimental facts, including

- the linear temperature dependence of the resistivity $\Delta\rho_{ab}(T) \propto T$ for $T > T_c$ (electron–phonon interaction);
- the absence of a coherence peak in the real part of the microwave conductivity $\sigma'_{ab}(T)$ (strong coupling), which is typical for classical superconductors when $0.8 < T < T_c$;
- the linear temperature dependences of $\Delta\lambda_{ab}(T) \propto T$ and $\Delta R_{ab}(T) \propto T$ for $T < T_c/4$ (predominant d-wave component of the order parameter);

- the different slopes of the $\lambda_{ab}(T)$ curves as $T \ll T_c$ and their inflection at $T \sim T_c/2$ in YBa₂Cu₃O_{6.93} crystals [an indication of (d + s)-symmetry of the superconducting gap, confirmed by calculations of $\lambda_{ab}(T)$ within the model of mixed symmetry of the order parameter in HTSCs].

In the absence of a generally accepted microscopic theory, I have shown that all peculiarities of the temperature dependences of the surface impedance and conductivity in the ab -planes of HTSC crystals with different chemical compositions are adequately characterized in the framework of the modified two-fluid model that accounts for quasiparticle scattering, inhomogeneous broadening of the superconducting transition, and variation of the density of superconducting carriers that is proportional to the temperature.

It was experimentally proved that the condition $R_{ab}(T) = X_{ab}(T)$ with $T > T_c$ for the normal skin effect is

valid for optimally doped YBCO, TBCCO, and BSCCO crystals but is violated for TBCO. A possible reason for this failure is a shielding effect of the microwave magnetic field by roughnesses in a TBCO crystal, formed by the cleavage plane traces on its surface.

It was shown that the large residual losses $R_{\text{res}} = R(T \rightarrow 0) \sim 100 \mu\Omega$ at a frequency of about 10 GHz in HTSCs, which exceed the R_{res} value in classical superconductors by a factor of several dozen, can be caused by the layered structure of HTSCs where the current in the surface layer of the crystal flows in a nonsuperconducting portion of the layer possessing a small but finite resistivity.

It was proved that the optimally doped $\text{YBa}_2\text{Cu}_3\text{O}_{6.93}$ is a 3D anisotropic metal: both components $\rho_{ab}(T)$ and $\rho_c(T)$ of the resistivity rise with an increase in temperature $T > T_c$ and, unlike BSCCO, the $\sigma_c(T) = 1/\rho_c(T)$ values in the normal state of YBCO exceed the lower limit for the c -axis conductivity of the 3D anisotropic metal. A slight decrease in the oxygen content ($7 - x$) of $\text{YBa}_2\text{Cu}_3\text{O}_{7-x}$ in comparison with the optimal level results in a crossover from 3D metallic conductivity to 2D Drude conductivity in CuO_2 layers and tunneling conductivity between these layers. From the numerical criterion obtained it follows that the 3D–2D crossover arises when the value of $\rho_c \rho_{ab} \approx 10^{-6} \Omega^2 \text{cm}^2$ is reached. The $\rho_c(T)$ dependences measured at different x can be described well by the polaron model of hopping quasiparticle c -transport allowing for the effects of strong electron–phonon interaction in the cuprate planes.

The behavior of the superfluid density $n_s(T, p) \propto \sigma_{ab}''(T, p)$ was investigated in $\text{YBa}_2\text{Cu}_3\text{O}_{7-x}$ crystals with the oxygen deficiency varied over the range $0.07 \leq x \leq 0.47$, which corresponds to the concentration of holes per copper atom in a CuO_2 plane in the range $0.16 > p > 0.07$. It was found that (i) as $T \rightarrow 0$ the superfluid density $n_s(0, p)$ depends linearly on p , $n_s(0, p) \propto p$; (ii) the slope of the $n_s(T, p)$ curves for $T \ll T_c$ depends slightly on p in the range $0.16 > p > 0.10$ but it increases rapidly with further p lowering, and (iii) the slope increase is accompanied by a change from the linear temperature dependence $n_s(T, p) \propto (-T)$ for $T < T_c/3$ to the square-root one, $n_s(T, p) \propto (-\sqrt{T})$. All these experimental facts are in favor of the DDW model of the pseudogap in HTSCs. It is experimentally proved that peculiarities in the temperature dependence of the imaginary part $\sigma_c''(T, p)$ of the c -axis conductivity for $T \ll T_c$ are not influenced by the DDW pseudogap. Their behavior is determined by a strong decrease in the interlayer coupling integral with a decrease in concentration p .

Although the above-mentioned results refer to the topical problems of HTSCs, they do not include two important lines of investigation:

(1) Experiments at ultra-low temperatures (however curious this might be for high- T_c superconductors).

The linear temperature dependence of the field penetration depth in the ab -plane of optimally doped HTSC crystals over the range $2 < T < 25$ K cannot extend down to the very close vicinity of $T = 0$, in accordance with the third law of thermodynamics [126]. It is unknown how this dependence would change for $T < 2$ K.

Measurements of $n_s(T)$ for $T < 2$ K in high-quality samples with low carrier densities, which are within the range of the superconductor–insulator transition in the HTSC phase diagram, are necessary in order to reach ultimate conclusions about the pseudogap model.

(2) Experiments in ultra-high magnetic fields.

High-precision measurements of the surface impedance and complex conductivity of HTSC crystals in magnetic fields $H > 15$ T have not been performed up to now and, hence, high-frequency methods of studying the Fermi surface that are far more accurate compared to angle-resolved photoemission spectroscopy (ARPES) are still in progress. They will require the creation of a new technique of microwave spectroscopy based on dielectric (e.g., prepared from monocrystalline sapphire) cavities which have, among the known resonance systems, the highest quality factor in a wide temperature range, regardless of the value of a magnetic field.

Interesting discoveries in this field of research can be expected in the nearest future, and it seems likely that further studies of the microwave response of HTSCs will develop in these two areas.

I am grateful to Yu A Nefedov, A F Shevchun, and A M Shuvaev for their collaboration and professionalism, V F Gantmakher for his comprehensive support, and A A Golubov and E G Maksimov for their fruitful discussions.

These studies are carried out with the support of the RFBR (project 03-02-16812) and the scientific programs of the RAS.

References

1. Bardeen J, Cooper L N, Schrieffer J R *Phys. Rev.* **108** 1175 (1957)
2. Xie Y B *Phys. Rev. B* **45** 11375 (1992)
3. Trunin M R, Golubov A A, in *Spectroscopy of High- T_c Superconductors. A Theoretical View* (Ed. N M Plakida) (London: Taylor & Francis, 2003) p. 159
4. Mao J et al. *Phys. Rev. B* **51** 3316 (1995)
5. Srikanth H et al. *J. Phys. Chem. Solids* **59** 2105 (1998)
6. Nefyodov Yu A et al. *Phys. Rev. B* **67** 144504 (2003)
7. Hosseini A et al. *Phys. Rev. Lett.* **81** 1298 (1998)
8. Jacobs T et al. *Phys. Rev. Lett.* **75** 4516 (1995)
9. Shibauchi T et al. *Physica C* **264** 227 (1996)
10. Lee S-F et al. *Phys. Rev. Lett.* **77** 735 (1996)
11. Shovkun D V et al. *Pis'ma Zh. Eksp. Teor. Fiz.* **71** 132 (2000) [*JETP Lett.* **71** 92 (2000)]
12. Zhukov A A et al. *Zh. Eksp. Teor. Fiz.* **112** 2210 (1997) [*JETP* **85** 1211 (1997)]
13. Broun D M et al. *Phys. Rev. B* **56** R11443 (1997)
14. Waldram J R et al. *Phys. Rev. B* **59** 1528 (1999)
15. Nefedov Yu A, Thesis for Candidate of Physicomathematical Sciences (Chernogolovka: Institute of Solid State Physics, RAS 2003)
16. Bonn D A et al. *Phys. Rev. Lett.* **68** 2390 (1992)
17. Bonn D A et al. *Phys. Rev. B* **47** 11314 (1993)
18. Bonn D A et al. *Phys. Rev. B* **50** 4051 (1994)
19. Kitano H et al. *Phys. Rev. B* **51** 1401 (1995)
20. Trunin M R et al. *Pis'ma Zh. Eksp. Teor. Fiz.* **65** 893 (1997) [*JETP Lett.* **65** 938 (1997)]
21. Srikanth H et al. *Phys. Rev. B* **55** R14733 (1997)
22. Srikanth H et al. *Phys. Rev. B* **57** 7986 (1998)
23. Kamal S et al. *Phys. Rev. B* **58** R8933 (1998)
24. Hosseini A et al. *Phys. Rev. B* **60** 1349 (1999)
25. Quinlan S M, Scalapino D J, Bulut N *Phys. Rev. B* **49** 1470 (1994)
26. Eliashberg G M *Zh. Eksp. Teor. Fiz.* **38** 966 (1960) [*Sov. Phys. JETP* **11** 696 (1960)]; *Pis'ma Zh. Eksp. Teor. Fiz.* **48** 275 (1988) [*JETP Lett.* **48** 305 (1988)]
27. Pickett W E *J. Supercond.* **4** 397 (1991)
28. Ginzburg V L, Maksimov E G *Sverkhprovodimost': Fiz., Khim., Tekh.* **5** 1543 (1992) [*Supercond.: Phys. Chem. Technol.* **5** 1505 (1992)]
29. Golubov A A et al. *J. Phys. I (France)* **6** 2275 (1996)
30. Bille A, Scharnberg K *J. Phys. Chem. Solids* **59** 2110 (1998)
31. Varma C M et al. *Phys. Rev. Lett.* **63** 1996 (1989)
32. Abrahams E *J. Phys. I (France)* **6** 2191 (1996)
33. Anderson P W *Physica C* **185–189** 11 (1991)

34. Anderson P W *The Theory of Superconductivity in the High- T_c Cuprates* (Princeton, NJ: Princeton Univ. Press, 1997)
35. Lee P A *Phys. Rev. Lett.* **71** 1887 (1993)
36. Hensen S et al. *Phys. Rev. B* **56** 6237 (1997)
37. Trunin M R et al. *Pis'ma Zh. Eksp. Teor. Fiz.* **64** 783 (1996) [*JETP Lett.* **64** 832 (1996)]
38. Fink H J *Phys. Rev. B* **58** 9415 (1998)
39. Xiang T, Panagopoulos C, Cooper J R *Int. J. Mod. Phys. B* **12** 1007 (1998)
40. Sridhar S, Kennedy W L *Rev. Sci. Instrum.* **59** 531 (1988)
41. Trunin M R *Usp. Fiz. Nauk* **168** 931 (1998) [*Phys. Usp.* **41** 843 (1998)]; *J. Supercond.* **11** 381 (1998)
42. Brandt E H, Mikitik G P *Phys. Rev. Lett.* **85** 4164 (2000)
43. Landau L D, Lifshitz E M *Elektrodinamika Sploshnykh Sred* (Electrodynamics of Continuous Media) (Moscow: Fizmatlit, 1982) [Translated into English (Oxford: Pergamon Press, 1984)]
44. Maeda A et al. *J. Low Temp. Phys.* **105** 323 (1996)
45. Kitano H, Hanaguri T, Maeda A *Phys. Rev. B* **57** 10946 (1998)
46. Bonn D A et al. *J. Phys. Chem. Solids* **56** 1941 (1995)
47. Asaoka H et al. *Jpn. J. Appl. Phys.* **32** 1091 (1993)
48. Gough G E, Exon N J *Phys. Rev. B* **50** 488 (1994)
49. Trunin M R et al. *J. Supercond.* **14** 181 (2001)
50. Erb A, Walker E, Flükiger R *Physica C* **258** 9 (1996)
51. Meingast C et al. *Phys. Rev. Lett.* **67** 1634 (1991)
52. Panagopoulos C et al. *Phys. Rev. Lett.* **79** 2320 (1997)
53. Nefyodov Yu A, Trunin M R *Physica C* **388**–**389** 469 (2003)
54. Tallon J L et al. *Phys. Rev. B* **51** 12911 (1995)
55. Shibauchi T et al. *Physica C* **203** 315 (1992)
56. Achkar D et al. *Phys. Rev. B* **48** 13184 (1993)
57. Shibauchi T et al. *J. Phys. Soc. Jpn.* **65** 3266 (1996)
58. Shibauchi T et al. *Phys. Rev. Lett.* **72** 2263 (1994)
59. Kusko C et al. *Phys. Rev. B* **65** 132501 (2002)
60. Ovchinnikov Yu N, Kresin V Z *Phys. Rev. B* **65** 214507 (2002)
61. Trunin M R *Pis'ma Zh. Eksp. Teor. Fiz.* **72** 845 (2000) [*JETP Lett.* **72** 583 (2000)]
62. Mende F F, Spitsyn A I *Poverkhnostnyi Impedans Sverkhprovodnikov* (Surface Impedance of Superconductors) (Kiev: Naukova Dumka, 1985)
63. Radtke R J, Levin K *Physica C* **250** 282 (1995); Rojo A G, Levin K *Phys. Rev. B* **48** 16861 (1993)
64. Kumar N, Jayannavar A M *Phys. Rev. B* **45** 5001 (1992)
65. Ioffe L B et al. *Phys. Rev. B* **47** 8936 (1993)
66. Graf M J, Rainer D, Sauls J A *Phys. Rev. B* **47** 12089 (1993)
67. Turlakov M, Leggett A J *Phys. Rev. B* **63** 064518 (2001)
68. Turlakov M, cond-mat/0111136
69. Trunin M R, Nefedov Yu A *Pis'ma Zh. Eksp. Teor. Fiz.* **77** 696 (2003) [*JETP Lett.* **77** 592 (2003)]; cond-mat/0306158
70. Ho A F, Schofield A J, cond-mat/0211675; *Phys. Rev. B* **71** 045101 (2005); cond-mat/0407059
71. Lang I G, Firsov Yu A *Zh. Eksp. Teor. Fiz.* **43** 1843 (1962) [*Sov. Phys. JETP* **16** 1301 (1963)]
72. Holstein T *Ann. Phys. (New York)* **8** 343 (1959)
73. Trunin M R, Nefyodov Yu A, Fink H J *Zh. Eksp. Teor. Fiz.* **118** 923 (2000) [*JETP* **91** 801 (2000)]
74. Fink H J, Trunin M R *Physica B* **284**–**288** 923 (2000); Fink H J *Phys. Rev. B* **61** 6346 (2000); Fink H J, Trunin M R *Phys. Rev. B* **62** 3046 (2000)
75. Gorter G J, Casimir H *Phys. Z.* **35** 963 (1934)
76. Turneure J P, Halbritter J, Schwettman H A *J. Supercond.* **4** 341 (1991)
77. Hein M, Kaiser T, Müller G *Phys. Rev. B* **61** 640 (2000)
78. Hylton T L, Beasley M R *Phys. Rev. B* **39** 9042 (1989)
79. Portis A M, Cooke D W *Supercond. Sci. Technol.* **5** S395 (1992)
80. Halbritter J *J. Appl. Phys.* **68** 6315 (1990); **71** 339 (1992)
81. Vendik O G, Kozyrev A B, Popov A Yu *Rev. Phys. Appl. (France)* **25** 255 (1990)
82. Vendik O G et al. *Sverkhprovodimost': Fiz., Khim., Tekh.* **3** 2133 (1990) [*Supercond. Phys. Chem. Technol.* **3** 1573 (1990)]
83. Eliashberg G M, Klimovitch G V, Rylyakov A V *J. Supercond.* **4** 393 (1991)
84. Dolgov O V et al. *Solid State Commun.* **89** 827 (1994)
85. Millis A J, Monien H, Pines D *Phys. Rev. B* **42** 167 (1990); Monien H, Monthoux P, Pines D *Phys. Rev. B* **43** 275 (1991); Monthoux P, Balatsky A V, Pines D *Phys. Rev. B* **46** 14803 (1992)
86. Hirschfeld P J, Putikka W O, Scalapino D J *Phys. Rev. Lett.* **71** 3705 (1993); *Phys. Rev. B* **50** 10250 (1994)
87. Abrikosov A A *Physica C* **214** 107 (1993); **222** 191 (1994); **244** 243 (1995)
88. Santi G et al. *Physica C* **259** 253 (1996)
89. Kamimura H et al. *Phys. Rev. Lett.* **77** 723 (1996)
90. Hettler M H, Hirschfeld P J *Phys. Rev. B* **61** 11313 (2000)
91. Berlinsky A J et al. *Phys. Rev. B* **61** 9088 (2000)
92. Durst A C, Lee P A *Phys. Rev. B* **62** 1270 (2000)
93. Combescot R, Leyronas X *Phys. Rev. Lett.* **75** 3732 (1995)
94. O'Donovan C, Carbotte J P *Phys. Rev. B* **52** 4568 (1995); **55** 8520 (1997)
95. Kim H, Nicol E J *Phys. Rev. B* **52** 13576 (1995)
96. Béal-Monod M T, Maki K *Phys. Rev. B* **53** 5775 (1996); **55** 1194 (1997)
97. Pokrovsky S V, Pokrovsky V L *Phys. Rev. B* **54** 13275 (1996)
98. Modre R, Schürer I, Schachinger E *Phys. Rev. B* **57** 5496 (1998)
99. Nefyodov Yu A et al. *Physica B* **284**–**288** 919 (2000)
100. Timusk T, Statt B *Rep. Prog. Phys.* **62** 61 (1999)
101. Tallon J L, Loram J W *Physica C* **349** 53 (2001)
102. Sadovskii M V *Usp. Fiz. Nauk* **171** 539 (2001) [*Phys. Usp.* **44** 515 (2001)]
103. Norman M R, Pépin C *Rep. Prog. Phys.* **66** 1547 (2003)
104. Loram J W et al. *J. Phys. Chem. Solids* **62** 59 (2001)
105. Bernhard C et al. *Phys. Rev. Lett.* **86** 1614 (2001)
106. Lee P A, Wen X-G *Phys. Rev. Lett.* **78** 4111 (1997)
107. Millis A J et al. *J. Phys. Chem. Solids* **59** 1742 (1998)
108. Ioffe L B, Millis A J *J. Phys. Chem. Solids* **63** 2259 (2002)
109. Bonn D A et al. *Czech. J. Phys.* **46** 3195 (1996)
110. Panagopoulos C, Cooper J R, Xiang T *Phys. Rev. B* **57** 13422 (1998)
111. Ding H et al. *Nature* **382** 51 (1996)
112. Kosztin I et al. *Phys. Rev. B* **61** 11662 (2000)
113. Stajic J et al. *Phys. Rev. B* **68** 24520 (2003)
114. Chakravarty S et al. *Phys. Rev. B* **63** 094503 (2001)
115. Tewari S et al. *Phys. Rev. B* **64** 224516 (2001)
116. Kim W et al. *Phys. Rev. B* **65** 064502 (2002)
117. Trunin M R, Nefyodov Yu A, Shevchun A F *Phys. Rev. Lett.* **92** 067006 (2004)
118. Uemura Y J *Physica C* **282**–**287** 194 (1997)
119. Wang Q-H, Han J H, Lee D-H *Phys. Rev. Lett.* **87** 077004 (2001)
120. Nayak C, Pivovarov E *Phys. Rev. B* **66** 064508 (2002)
121. Trunin M R, Nefyodov Yu A, Shevchun A F *Supercond. Sci. Technol.* **17** 1082 (2004)
122. Radtke R J, Kostur V N, Levin K *Phys. Rev. B* **53** R522 (1996)
123. Hirschfeld P J, Quinlan S M, Scalapino D J *Phys. Rev. B* **55** 12742 (1997); Chakravarty S, Kee H-Y, Abrahams E *Phys. Rev. Lett.* **82** 2366 (1999); Ohashi Y J. *Phys. Soc. Jpn.* **69** 659 (2000)
124. Basov D N et al. *Phys. Rev. B* **50** 3511 (1994); Kirtley J R et al. *Phys. Rev. Lett.* **81** 2140 (1998); Dordevic S V et al. *Phys. Rev. B* **65** 134511 (2002)
125. Nyhus P et al. *Phys. Rev. B* **50** 13898 (1994)
126. Schopohl N, Dolgov O V *Phys. Rev. Lett.* **80** 4761 (1998); Volovik G E *Phys. Rev. Lett.* **81** 4023 (1998); Hirschfeld P J, Li M-R, Wölfle P *Phys. Rev. Lett.* **81** 4024 (1998)